



Challenging asymmetric cements as indicators of vadose diagenesis: “pseudo-gravitational” cements from the lower Pliensbachian of the Traras Mountains in NW Algeria

Salim Belkhedim^{1,2} · Axel Munnecke² · Miloud Benhamou¹ · Abdelkrim Nemra³ · Radouane Sadji¹

Received: 18 August 2018 / Accepted: 17 January 2019
© Springer-Verlag GmbH Germany, part of Springer Nature 2019

Abstract

Asymmetric, pendant cements are considered good indicators for early lithification in the vadose zone. In the present study, asymmetric cements are recorded in thin-sections of a Lower Jurassic limestone from the Traras Mountains (northwest Algeria). Geopetal fabrics, however, indicate that these seemingly “pendant cements” are, in some places, oriented upwards, i.e., they have grown in the opposite direction from that expected, or they grew from grains towards the pore centers. These observations disprove their origin as gravitational cements precipitated from pendant water droplets on the undersides of grains as in the vadose zone. In contrast, a formation in the marine phreatic zone seems more probable. Under high-energy conditions, and after an early lithification stage with isopachous cements in the subtidal zone, strong tidally driven horizontal pore-water flow allowed sufficient seawater to pass through the slightly cemented but still highly permeable rock. Those grain sides, which were oriented towards the pore center, where faster flowing water prevailed, were more exposed to CaCO₃-supersaturated percolating seawater and therefore the cements precipitated here show their greatest thickness. In relatively more protected areas around the margins of the pores, asymmetric cements are rarely developed. The resulting rock exhibits an unusual, heterogeneous cementation with preferential centripetal nucleation areas.

Keywords Geopetal fabrics · Horizontal permeability · Phreatic zone · Early lithification · Centripetal nucleation

Introduction

Microscopic studies of carbonate cements provide visual information with respect to the diagenetic environments in which the rocks have been lithified or altered (Schneidermann and Harris 1985). Isopachous needle-shaped (acicular or fibrous) cements distributed around sedimentary components with more or less equal thickness are interpreted as precipitated when the pores were completely filled with

seawater, thereby indicating formation in subtidal conditions (e.g., Flügel 2010). Reliable indicators for an early diagenetic lithification in a vadose setting are meniscus cements and pendant cements, the latter also called gravitational, microstalactitic or dripstone cements (e.g., Scholle and Ulmer-Scholle 2003; Flügel 2010). In such environments, pores are only periodically and partially water-filled (e.g., Hood and Wallace 2012; Andrieu et al. 2018; Christ et al. 2018), and the selective collection of water on the undersides of grains as pendant droplets is driven principally by gravitational drainage (Tucker and Wright 1990; Collin et al. 2009). After multiple phases of drainage and precipitation, visible asymmetric cements will develop beneath the grains, in the same positions as occupied by the water droplets (Scholle and Ulmer-Scholle 2003; Moore 2004). Thus, the thickest part of the cements is directed downward, and they thin towards the upper sides of the grains. The mineralogy and thus the shape of the pendant cement crystals depends on the Mg/Ca ratio of the fluid from which they have been precipitated (Molenaar and Venmans 1993; Flügel 2010). In view of the high Mg/Ca ratio of seawater, pendant cements in the

✉ Salim Belkhedim
saligeol@gmail.com

¹ Laboratoire de Géodynamique des Bassins et Bilan Sédimentaire, Université Mohamed Ben Ahmed Oran 2, 1524 El M'naouer, 31000 Oran, Algeria

² GeoZentrumNordbayern, FachgruppePaläoumwelt, University of Erlangen-Nuremberg, Loewenichstr. 28, 91054 Erlangen, Germany

³ Laboratoire de Paléontologie Stratigraphie et Paléoenvironnement, Université Mohamed Ben Ahmed Oran 2, 1524 El M'naouer, 31000 Oran, Algeria

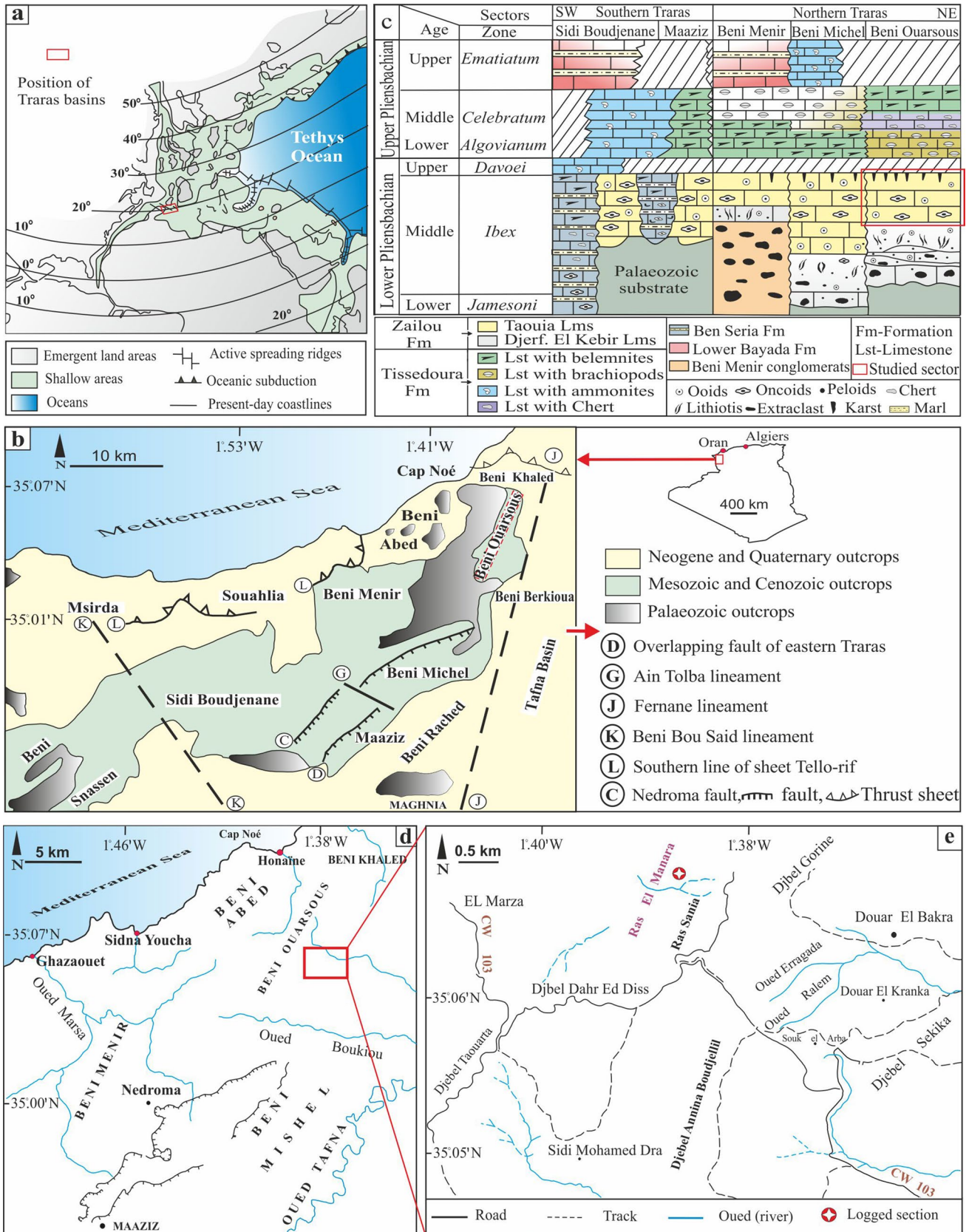


Fig. 1 Geological setting of the Traras Mountains and geographic position of the studied area. **a** Position of Traras basins in the Pliensbachian. **b** Simplified geological map of the Traras Mountains. **c** Lithostratigraphic subdivision of the Traras Mountains during the Pliensbachian (after Ameur 1999). **d** Geographic position of the studied sector. **e** Position of the Ras El Manara section

vadose marine zone are formed by needle-shaped aragonite or high magnesium calcite (HMC) crystals. Precipitation of CaCO_3 from seawater is enhanced by evaporation during low tide or after storm surges, and by CO_2 degassing and evaporation of sea spray in the splash zone (Molenaar and Venmans 1993). In contrast, pendant cements formed in the meteoric vadose zone consist of equant low-magnesium calcite crystals (LMC) because of the low Mg/Ca ratio of fresh water. The influence of meteoric diagenesis commonly results in a variable luminescence of cements under CL, indicating changes from reduced to oxidized fluids (Christ et al. 2015; Godet et al. 2016; López-Quirós et al. 2016; Andrieu et al. 2018; Christ et al. 2018).

Thin-sections of a Lower Jurassic limestone from the Ras El Manara section (Zailou Formation) in the Traras Mountains (northwest Algeria) reveal asymmetric cements resembling gravitational cements. However, the presence of numerous geopetal fabrics highlights the fact that these seemingly “pendant cements” are oriented in various directions, some of them are even oriented upwards, contrary to a gravitational cement interpretation. Topics of the present paper are a detailed description of these unusual asymmetric cements, a determination of their nature, whether vadose or phreatic, and finally a development of a hypothesis explaining their formation.

Geological and geographical situation

The studied area is a part of the Traras Mountains, which belonged to the northern margin of the Tlemcen Domain in the Western Tethys (Fig. 1a). The Traras Mountains acquired their major structural features before the Middle Miocene transgression after several tectonic events (Guardia 1975). Today, they are located in northwest Algeria and represent the continuation of the Moroccan Béni Snassène Mountains. They are limited to the north by the Mediterranean Sea, to the east by the Tafna valley, to the west by the eastern part of Béni Snassène, and to the south by the Maghnia depression (Fig. 1b).

The Traras Mountains are formed of a Paleozoic basement, covered by Mesozoic, Cenozoic, and Quaternary sedimentary deposits. Carbonate deposits accumulated in the Early and Middle Jurassic, from the early Pliensbachian to the early Bathonian (Ameur 1999). The first Jurassic sea flooded the Tlemcen Domain during the early Pliensbachian

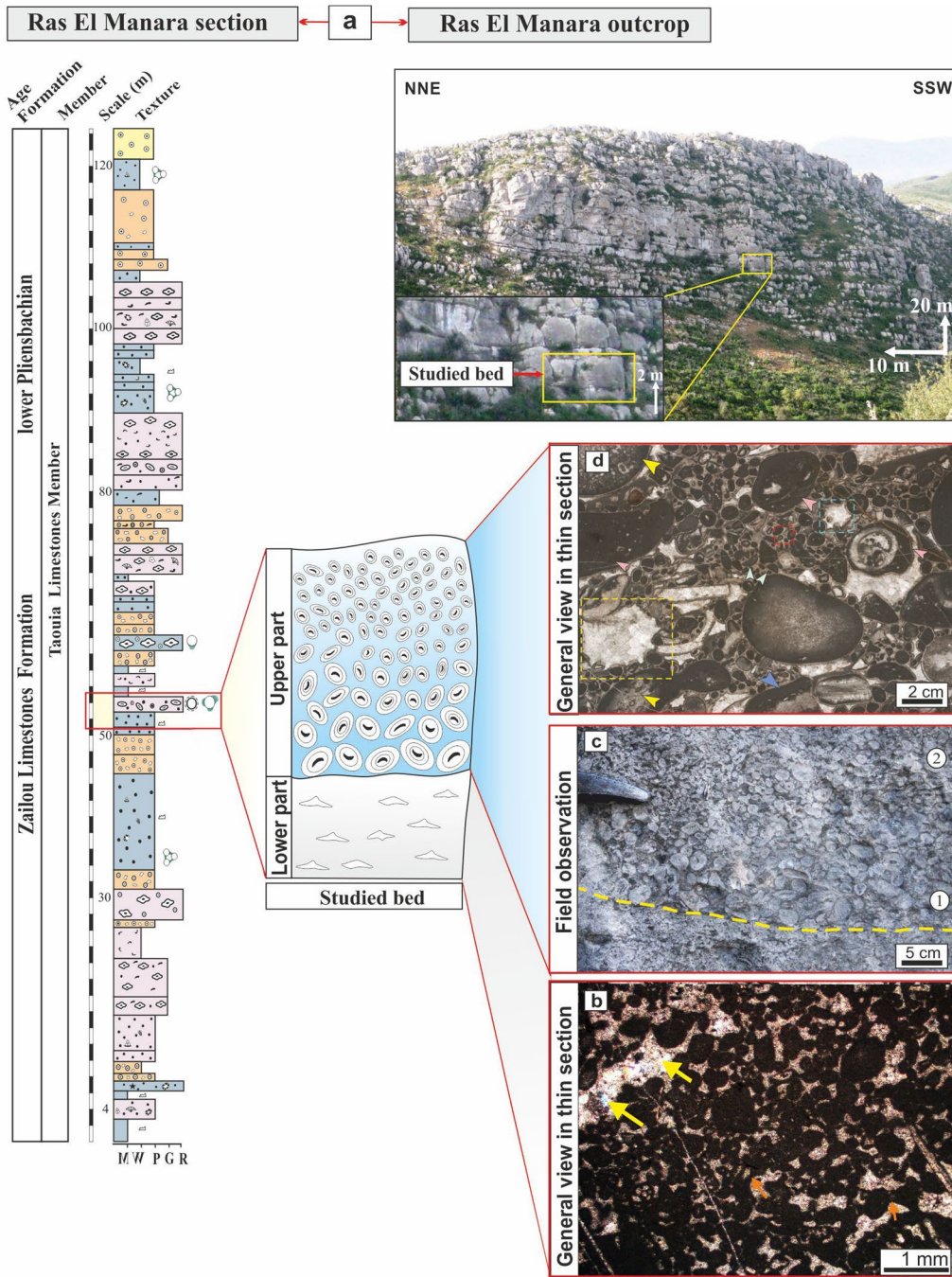
along depressions created by the first stage of the Tethys seafloor spreading. During this time, the Traras Mountains were divided into at least three distinct basins, showing steep and rapid transitions between them (commonly within less than 1 km) (Elmi et al. 2009). Each of these basins is represented by a mosaic of sub-basins, separated by shoal areas. Shallow inner-platform deposits accumulated (Zailou Limestones Formation) that are thick in the basins and thin in marginal shallow sand-shoals. In the late Pliensbachian, a second fragmentation took place in the region of the Traras Mountains. Outer platform environments developed and they are now represented by the Tissedouira Formation (Fig. 1c), which consists of cherty limestones with an ammonite and brachiopod fauna. At the end of the late Pliensbachian, the western areas were characterized by an ongoing deepening and consequently the deposition of outer platform carbonates (basal deposits of the Bayada Fm), while the eastern Traras Mountain area was elevated, with little or no sedimentation (Fig. 1c).

The studied section “Ras El Manara” (120 m) occupied the northern part of the Dahr Diss massif. This massif belongs to the Beni Ouarsous sector, located in the northern part of the Traras Mountains (Fig. 1c, d). The GPS coordinates are $35^{\circ}7'50.69''\text{N}$ – $1^{\circ}38'41.00''\text{W}$ (Fig. 1e). The section consists only of the Taouia Limestone Member of the Zailou Formation and exposes the upper part of the middle lower Pliensbachian *Ibex* zone (Fig. 1c) (Ameur 1999). No younger sediments are exposed in this area.

Materials and methods

Petrography and diagenesis

The studied limestone bed crops out in the middle part of the Ras El Manara section (lower Pliensbachian) (Figs. 1c, 2a). Facies determination and environmental interpretation of the Ras El Manara section are based on field observations, and a petrographic study of 71 thin-sections stained with alizarin–potassium ferricyanide in order to distinguish between ferrous and ferric iron incorporated in the calcite lattice (Dickson 1966). Several samples were taken from the upper part of the studied bed and six additional thin-sections were cut in the vertical plane. Facies and diagenesis were studied in transmitted and polarized light using an optical microscope, and by cathodoluminescence (CL) microscopy, in order to characterize early cement features. The CL analyses were carried out at the GeoZentrum Nordbayern, Friedrich-Alexander-Universität Erlangen-Nürnberg (Germany), using a Technosyn 8200 MK II luminescope system operating under 14–16-kV accelerating voltage and 200–300- μA beam current.



| Skeletal components | Non skeletal Components | Main facies association | Cements and diagenetic features | Textures |
|---|---|--|---|---|
| <ul style="list-style-type: none"> Reworked <i>Lithotia</i> Foraminifera Gastropods Crinoids Bioclasts Corals Green algae Cyanobacteria | <ul style="list-style-type: none"> Oncoids Oncoids with smooth surface Superficial oncoids Ooids Peloids Extraclasts Gypsum | <ul style="list-style-type: none"> Inter-supratidal Shallow proximal lagoon Protected/high energy open lagoon Shoal/transition | <ul style="list-style-type: none"> Meniscus cement Pendant cement Asymmetric cement Isopachous cement Fenestrate fabrics Stylolites | <ul style="list-style-type: none"> M : Mudstone W : Wackestone P : Packstone G : Grainstone R : Rudstone |

Fig. 2 a Ras El Manara outcrop and section. **b** In thin-section, the lower part of the studied bed is a peloidal packstone with micritic meniscus cements (orange arrows) and keystone vugs (yellow arrows). **c** Field observation of the studied interval. Oncoids with normal grading deposited upon an erosional surface. **d** General view of the studied interval in thin-section with rounded oncoids (pink arrows), some of them are broken (blue arrows), embedded within an ooidal grainstone with some bioclasts (yellow arrows) (see the text for more detailed description). The ooids are also broken in some places (green arrows). Three types of pore can be distinguished: large (3–12 mm; yellow dished square), medium (1–3 mm; blue dished square, and small (< 1 mm; red dished square)

Geochemical analysis

Stable carbon and oxygen isotopes have been measured from 40 bulk samples (Fig. 3a; Table 1). In order to reconstruct the early diagenetic environments of the recorded asymmetric cements, four samples from the asymmetric fibrous cements (AFC) and two from isopachous fibrous cements I (IFC-I) were sampled using a microscope-mounted micro-drill. For comparison, six additional samples from the same thin-sections were drilled; three from sparry calcite cements and three from different grains (oncoids, coral fragments) (Fig. 3b; Table 2). In view of their small sizes, no samples were taken from the isopachous fibrous cements II (IFC-II) or the dark sediments (DS). Both microdrilling and stable isotope analysis were carried out at the GeoZentrum Nordbayern, Friedrich-Alexander-Universität Erlangen-Nürnberg (Germany). About 5–10 mg of powder was obtained per sample. The powders were reacted with 100% phosphoric acid at 70 °C using a Gasbench II connected to a Thermo Finnigan Five Plus mass spectrometer. All values are reported in per mil relative to V-PDB by assigning $\delta^{13}\text{C}$ and $\delta^{18}\text{O}$ values of +1.95‰ and –2.20‰ to NBS19 and –46.6‰ and 26.7‰ to LSVEC, respectively. Reproducibility and accuracy were monitored by replicate analysis of laboratory standards calibrated to NBS19 and LSVEC and were better than $\pm 0.05\text{‰}$ (1σ) and $\pm 0.09\text{‰}$ (1σ), respectively.

Results

Paleoenvironmental setting of the Ras El Manara section

The Ras El Manara section (120 m) has been subdivided into 15 facies, grouped into four facies associations, namely inter-supratidal, restricted lagoon, open lagoon, and shoal (Fig. 4; Table 3). They are arranged into small-scale shallowing-upward cycles and were developed within inner-ramp environments above fair-weather wave base (Fig. 5). Each cycle is formed by subtidal deposits alternating with inter- to supratidal deposits. The subtidal portion of each cycle consists of restricted and open lagoonal deposits,

whereas fine-grained tidal flat deposits or beach deposits characterize the inter-supratidal environment (Fig. 2a). Detailed description, occurrence, and interpretation of the facies are summarized in Table 3.

Sedimentology of the studied bed (sample 24)

The studied limestone bed (sample 24; Figs. 2, 3) is laterally continuous and has a thickness of about 4 m. Its lower part is formed by peloidal packstone showing fenestral fabrics (keystone vugs) and micritic meniscus cements (Fig. 2b). It is truncated by an erosional surface (Fig. 2c). The upper part of the bed consists of ooidal grainstone and locally oncoidal rudstone facies, starting with large spherical oncoids (1–3 cm) with smooth surfaces (Fig. 2c1), and passing vertically, in normal grading, to small, rounded to subrounded oncoids (1 cm) (Fig. 2c2). In thin-section, the upper part of this bed shows abundant oncoids embedded within an ooidal grainstone “matrix” (Fig. 2d); these oncoids are spherical to subspherical and range in size from 1 to 2 cm. They show bioclastic nuclei and micritic cortices, alternating with organism-bearing laminae (porostromate layers). They have smooth surfaces and in some places are broken. The ooids are micritic, small (0.5–1.5 mm), well to moderately sorted, and some of them are also broken. Only a few bioclasts are present, represented commonly by reworked, rounded coral fragments. Other bioclasts are surrounded by thin micritic laminae, forming superficial oncoids (Fig. 2d). All the grains, with their different sizes, touch each other (point contacts), and create different pore-sizes (Fig. 2d). The intergranular space between grains is mostly filled by sparry blocky calcite and subordinate micrite (Fig. 2d).

Diagenesis and geochemical characteristics

The studied interval shows superimposition of several early diagenetic features, forming a polygenic discontinuity surface (Immenhauser et al. 2000) or composite surface (Sattler et al. 2005; Andrieu et al. 2018) (Table 4).

Isopachous fibrous cements I and II (IFC-I and IFC-II)

Two generations of isopachous fibrous cement have been observed. The first generation (IFC-I) is composed of isopachous fibrous fringes, which surround all the components (ooids, oncoids, and bioclasts) (Figs. 6a, c, e and 7h). The thicknesses range between 60 and 100 μm . A second generation of very thin isopachous fibrous cement (30–60 μm) (IFC-II) precipitated above a dark sediment (DS) (see below) (Figs. 6a, c, e and 7d, h). Both of these are non-ferroan as indicated by their pink color after alizarin–potassium ferricyanide staining. Under cathodoluminescence (CL), both exhibit no luminescence (Fig. 6b, d, f). The stable carbon

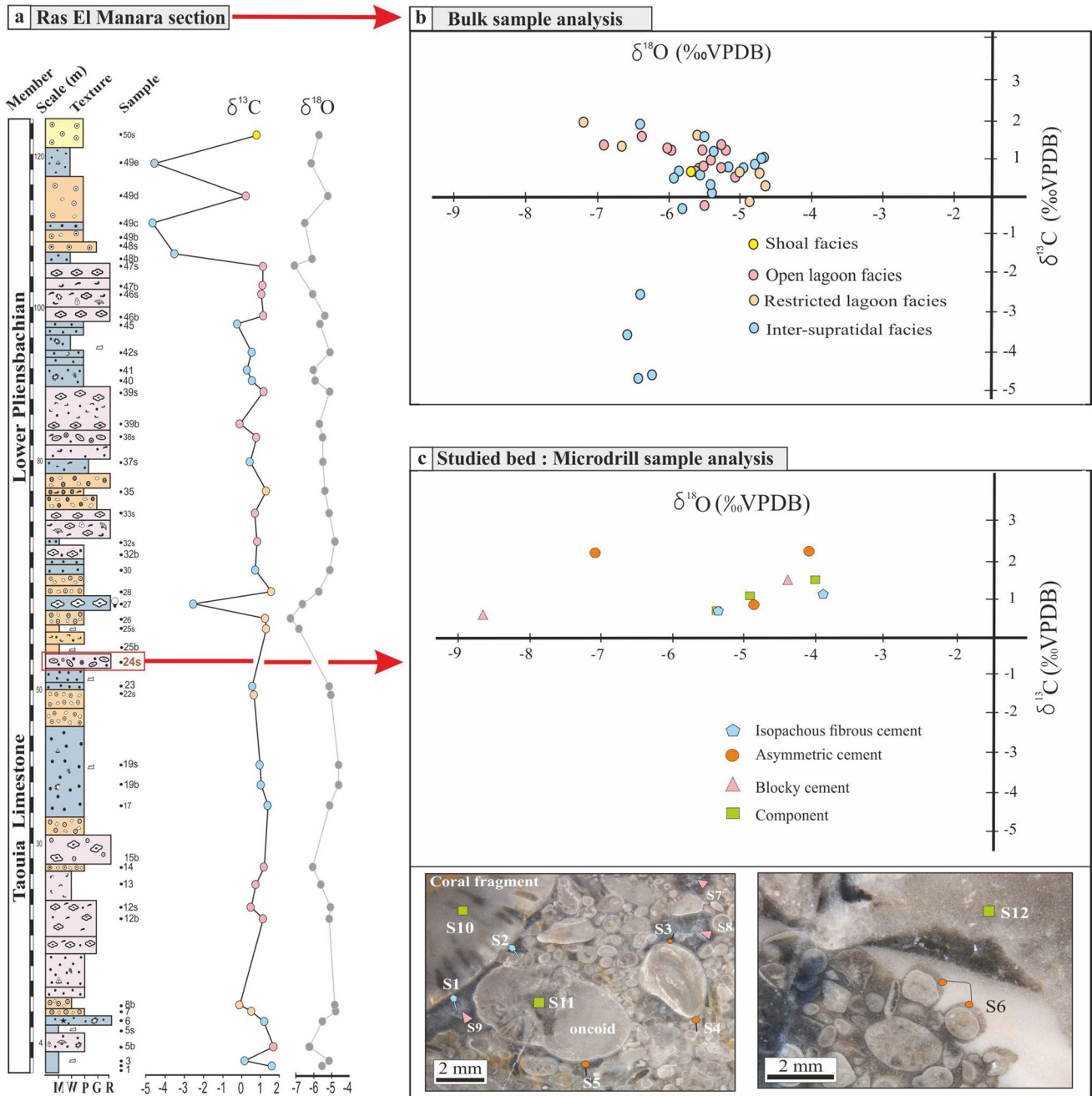


Fig. 3 a, b Carbon and oxygen isotope ratios of the whole Ras El Manara section in the lower Pliensbachian (bulk samples) (see Fig. 2 for legend explanation). c Carbon and oxygen isotope ratios of the

polished sample. The two photos below show the position of the sampled cements and grains in sample 24 (see Table 2 for number explanations)

isotope values for the IFC-I vary between +0.7 and +1.1%, and the oxygen isotope values between -3.9 and -5.3‰.

asymmetric cements (see below). In cathodoluminescence, it shows orange to red luminescence (Fig. 8f).

Dark sediments (DS)

Geopetal fabrics (GF)

Within the IFC, above IFC-I, a very thin dark zone is developed (Figs. 7 e, g, h; 8e). It is also observed within the

Geopetal micrite (GF) appears in several intergranular pores ranging in size between 600 μm and 11 mm. They are all consistent in their orientation with each other and

Table 1 Carbon and oxygen isotope composition (bulk samples) of the Ras El Manara section

| Samples | $\delta^{13}\text{C}$ (‰) | $\delta^{18}\text{O}$ (‰) |
|---------|---------------------------|---------------------------|
| R.M 2 | 1.72 | -5.55 |
| R.M 3 | 0.12 | -5.39 |
| R.M 5b | 1.89 | -6.40 |
| RM6 | 1.10 | -5.45 |
| R.M 7 | 0.68 | -4.84 |
| R.M 8b | -0.07 | -4.80 |
| R.M 12b | 1.15 | -5.21 |
| R.M 12s | 0.52 | -5.10 |
| R.M 13 | 0.78 | -5.62 |
| R.M 14 | 1.22 | -5.97 |
| R.M 17 | 1.48 | -5.25 |
| R.M 19b | 1.04 | -4.66 |
| R.M 19s | 1.00 | -4.68 |
| R.M 22s | 0.74 | -4.96 |
| R.M 23 | 0.64 | -5.17 |
| R.M 24b | 0.79 | -5.57 |
| R.M 25s | 1.33 | -6.67 |
| R.M 26 | 2.00 | -7.23 |
| R.M 27s | -2.46 | -6.40 |
| R.M 28 | 1.68 | -5.64 |
| R.M 30 | 0.79 | -5.27 |
| R.M32s | 0.77 | -4.78 |
| R.M 33s | 0.78 | -5.23 |
| R.M 35s | 1.36 | -5.35 |
| R.M 37s | 0.50 | -5.43 |
| R.M 38s | 0.89 | -5.44 |
| R.M 39b | -0.17 | -5.67 |
| R.M 39s | 1.19 | -5.28 |
| RM40 | 0.58 | -5.87 |
| RM41 | 0.37 | -5.96 |
| R.M 42s | 0.51 | -5.14 |
| R.M 45s | -0.18 | -5.61 |
| R.M 46b | 1.13 | -5.42 |
| R.M 46s | 1.01 | -5.38 |
| R.M 47m | 1.19 | -5.98 |
| R.M 47s | 1.28 | -6.90 |
| R.M 48m | -3.50 | -6.57 |
| RM49c | -4.64 | -6.41 |
| RM 49d | 0.20 | -5.38 |
| R.M 49e | -4.50 | -6.23 |
| RM50s | 0.70 | -5.69 |

with the bedding surfaces. The remaining voids above the geopetal micritic fillings are filled with sparry calcite (Figs. 6a, c, e and 7e, f), which displays an orange to red color under cathodoluminescence (Fig. 6b, d, f).

Table 2 Carbon and oxygen isotopic composition of different constituents in sample 24 (see Fig. 3 for precise sample positions)

| Grain/cement | Sample | $\delta^{13}\text{C}$ (‰) | $\delta^{18}\text{O}$ (‰) |
|-----------------------------------|--------|---------------------------|---------------------------|
| Isopachous fibrous cement (IFC-I) | S1 | 1.08 | -3.92 |
| Isopachous fibrous cement (IFC-I) | S2 | 0.68 | -5.33 |
| Asymmetric fibrous cement (AFC) | S3 | 2.32 | -7.08 |
| Asymmetric fibrous cement (AFC) | S4 | 2.40 | -4.20 |
| Asymmetric fibrous cement (AFC) | S5 | -0.09 | -5.87 |
| Asymmetric fibrous cement (AFC) | S6 | 0.96 | -4.95 |
| Sparry calcite cement | S7 | -1.46 | -5.80 |
| Sparry calcite cement | S8 | 0.55 | -8.65 |
| Sparry calcite cement | S9 | 1.51 | -4.32 |
| Grains (piece of coral) | S10 | 1.03 | -4.85 |
| Grain (oncoïd) | S11 | 0.7 | -5.34 |
| Grain (oncoïd) | S12 | 1.5 | -4.04 |

Asymmetrical fibrous cements (AFC)

Several grains exhibit strongly asymmetrical fibrous crusts with thicknesses ranging from 100 to 500 μm . They show two generations: a first generation (AFC-I) overgrowing the IFC-I and a second one (AFC-II) upon the IFC-II. Unlike gravitational dripstone cements, the thickest parts of these asymmetrical cement crusts do not show a common downward growth direction, but grew in various directions, usually towards the pore centers (centripetal growth) (Figs. 7d–h and 8c), but locally even upward (Figs. 6a, c, e and 7c, e, f). Moreover, in some cases they have nucleated on different sides of the same grain (Fig. 7e). The thickest asymmetrical cements are observed in larger pores (3–12 mm) (Figs. 6a and 7c, e–g), whereas they are rarer and thinner in medium-sized pores (Fig. 7d) (1–3 mm), and absent in small ones (< 1 mm) (Fig. 9). In the CL, these cements are non-luminescent (Fig. 6b, d, f). Their stable carbon isotope values vary between -0.1 and +2.4‰, the oxygen isotope values between -4.2 and -7.1‰.

Aragonitic shells

Original aragonitic bioclasts such as corals and gastropods now consist of dogtooth cements, which show mostly no luminescence, than by two generations of granular calcite with variable luminescence (brown and bright). They do not show any relics of their original structure (Fig. 7b).

Dogtooth cements (DC)

Dogtooth cement have grown above the geopetal fabrics, around grains (Fig. 6d) and within dissolved bioclasts (Fig. 7b). They are formed by limpid scalenohedral crystals 100–150 μm in length and are not developed continuously

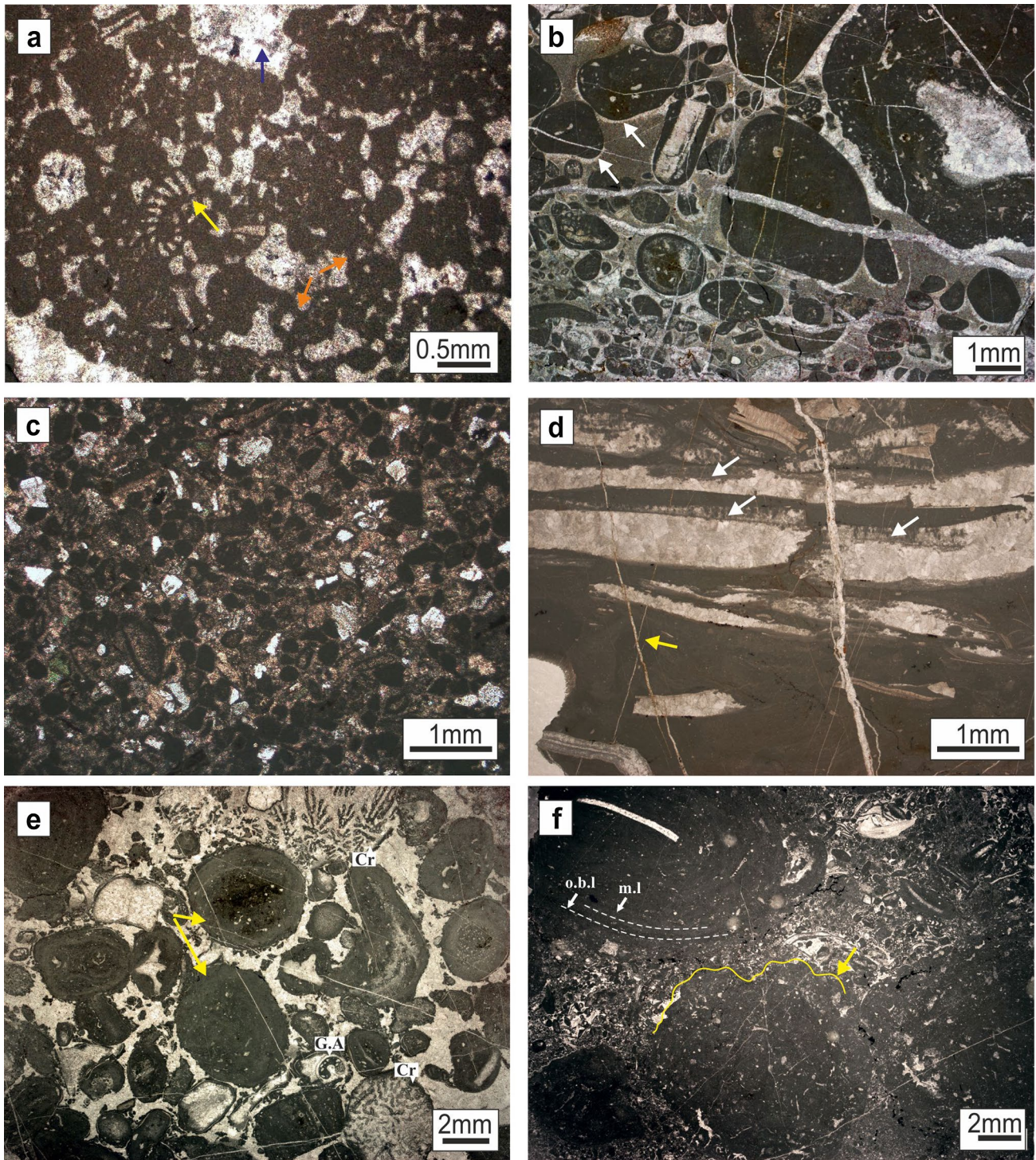


Fig. 4 Microfacies of the Ras El Manara section. **a** Peloidal packstone with benthic foraminifera (yellow arrow) micritic meniscus cement (orange arrows) (F1d; no 18). Note the presence of keystone vugs (blue arrow). **b** Oncoidal rudstone exhibiting needle-shaped pendant (gravitational) cements (arrows) indicating early lithification in the marine vadose zone (beach rock) (F2; no 27 s). **c** Mixed peloidal-quartz packstone. The peloids are rounded to surrounded, whereas the quartz grains show angular to subangular form (F3a; no 7). **d** *Lithioperla scutata* (bivalve) within micritic matrix, showing

micritization (white arrows), and microbial laminae (yellow arrows) (F3b; no 25). **e** Oncoidal-bioclasic rudstone (F4b; no 33b). The oncoids are micritic and spherical to subspherical, the bioclasts are corals (Cr), green algae (G.A), and crinoids. **f** Oncoidal rudstone with peloidal packstone matrix (F5c; no 39). The oncoids show bumpy surfaces (yellow arrow). They are characterized by micritic laminae (m.l.) alternating with organism-bearing laminae (o-b.l) (porostromate layers), or have an unlaminate meshwork

Table 3 Main facies and depositional environmental setting

| Facies | Component | Facies association |
|--|--|--|
| Inter-supratidal | | |
| F1a—homogenous micritic mudstone | Unfossiliferous burrowed micrite with birdseyes meniscus cements and geopetal fabrics, pyrite | Tidal flats |
| F1b—cyanobacteria dasycladacean rudstone | <i>Garwoodia</i> , green algae, well-sorted peloids (200 µm), aggregate grains, birdseyes and geopetal fabrics | |
| F1c—fenestrate laminated bindstone | Well-sorted tiny peloids alternating with micritic layers, lumpstone, fenestrate laminated fabrics | |
| F1d—fenestrate aggregate-peloidal packstone | Peloids (250 µm), lumpstone, elongated small oncoids, ooids, benthic foraminifera, keystone vugs (Fig. 4a) | |
| F2—oncoidal rudstone with pendant cement | Elliptical porostromate oncoids (0.5–1 cm) with bioclastic nuclei, poorly sorted ooids and peloids, <i>Cayeuxia</i> , cortoids, needle-shaped pendant cement (Fig. 4b) | Beach |
| Shallow restricted lagoon | | |
| F3a—mixed quartz-oidal-peloidal packstone | Tangential ooids, radial ooids (300 µm) moderately to well sorted peloids (200 µm), angular to subangular quartz (400 µm) (10–50%), cortoids, grapestone (Fig. 4c) | |
| F3b— <i>Lithotis</i> bivalves within micritic matrix | <i>Lithoperna scutata</i> genera embedded within micritic matrix, showing geopetal fabric, micritization, and microbial mats (Fig. 4d) | |
| Shallow open lagoon | | |
| F4a—Bioclastic-oncoidal rudstone | Gastropods, green algae, corals, benthic foraminifera, oncoids, peloids, ooids, cortoids, grapestone, <i>Solenopora</i> | Open lagoon with moderate to high energy |
| F4b—oncoidal-bioclastic rudstone | Micritic oncoids, spherical to subspherical, 1–2 cm in size, mixed with green algae, corals and crinoids (Fig. 4e) | |
| F4c—peloidal-bioclastic packstone | Rounded to subrounded peloids moderately sorted, mixed with gastropods, sponges, corals, echinoids spines, foraminifera, elliptical oncoids (1 cm), cortoids and grapestones | |
| F4d—oncoidal rudstone within ooidal grainstone | Porostromate oncoids (up to 6 mm) with smooth surface rudstone, embedded within radial and tangential ooids (700 µm), show | |
| F5a—peloidal packstone | Small, rounded to subrounded, moderately sorted peloids, benthic foraminifera | Open lagoon with low energy |
| F5b—asymmetrical oncooid-peloid rudstone | Elongated asymmetrical small oncoids (2–10 mm) with bioclastic nuclei, small peloids, well-sorted ooids and cortoids benthic foraminifera | |
| F5c—oncoidal rudstone with peloidal packstone matrix | Spherical and subspherical porostromate oncoids (1–3 cm), peloids ooids, aggregates, cortoids, corals, benthic foraminifera (Fig. 4f) | |
| F6a—tangential ooidal grainstone | Moderate- to well-sorted tangential ooids (500–800 µm) | Shoal |

around the grains. Except for the youngest parts, which show bright orange luminescence, these cements mostly display no luminescence (Fig. 6d). They are considered generally as LMC (Durllet and Loreau 1996; Andrieu et al. 2017).

Blocky calcite cements (BC)

Two generations of blocky calcite have been recognized. The first (Bc1) one is characterized by brown luminescence

surrounded by bright luminescence (Fig. 7b); the second (Bc2) one shows only brown luminescence (Fig. 7b).

Interpretation and discussion

Although resembling gravitational cements, which precipitate under a gravity control, the processes leading to the formation of the asymmetric cements (AFC) must be

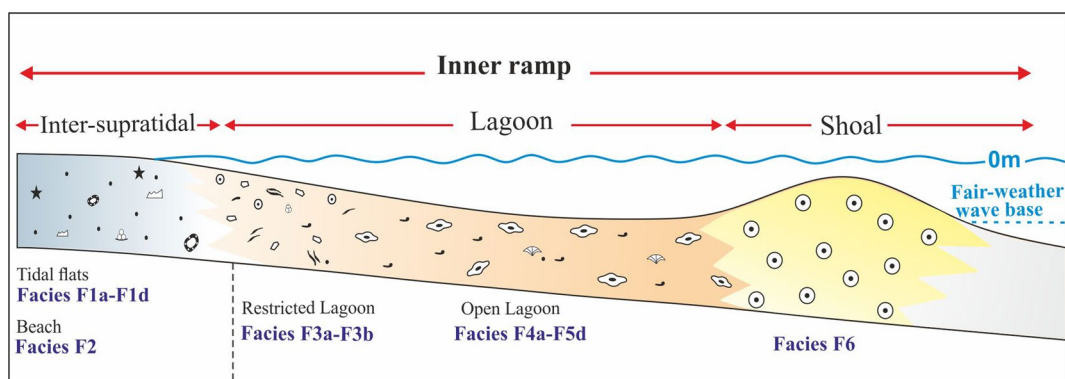


Fig. 5 Facies model and environmental reconstruction of the Ras El Manara section during the lower Pliensbachian

Table 4 Summarized petrographic characteristics of carbonate cements of the Ras El Manara section

| Diagenetic phase | Features | Cathodoluminescence | Occurrence |
|---|---|--|---|
| Isopachous fibrous cement I (IFC-I) | Fibrous cement, 60–100 μm in length, non-ferroan | Non-luminescent | Facies: F4d, sample: S24s |
| Isopachous fibrous cement II (IFC-II) | Fibrous cement, 60–100 μm in length, non-ferroan | Non-luminescent | Facies: F4d, sample: S24s |
| Asymmetric fibrous cement I and II (AFC-I and AFC-II) | Fibrous asymmetric crust of 100–500 μm in length and non-ferroan, centripetal growth | Non-luminescent | Facies: F4d, sample: S24s |
| Geopetal fabrics (GF) | Micrite 600 μm to 11 mm in length, followed by sparry calcite cements, non-ferroan | Orange to red luminescence | Facies: F1a–F1b; F4d, sample: S6, S24s |
| Dogtooth cement (DC) | Scalenoedral fringes or isolated crystals of 100–150 μm in length | Non-luminescent surrounded by bright yellow band | Facies: F4d, sample: S24s |
| Dark sediments (DS) | Fibrous cement 20–50 μm in length, non-ferroan | Orange to red luminescence | Facies: F4d, sample: S24s |
| Pendant cement (PC) | Fibrous asymmetric pendant crust of 100–300 μm in length and non-ferroan | Non-luminescent | Facies: F2, sample: S27s |
| Meniscus micritic cement (MMC) | Asymmetric micritic cement between grains, 100–200 μm in length | Orange to red luminescence | Facies: F1a–F1c, F4de sample: S6, S17–S20, S24b, S30, S32s, S40–S45, S49e |

completely different, because they grew in different directions. Thus, they neither reflect the original orientation of the strata nor a vadose diagenetic zone. The sedimentological and diagenetic history of this composite surface is interpreted as follows:

Step 1: Deposition of the sediment (Fig. 10a)

The investigated sediment is dominated by moderately sorted ooidal sands, admixed with some bioclasts and porostromate oncoids with smooth surfaces. Some of the oncoids are broken. The moderate sorting of the ooids indicates their reworking within the shallow proximal lagoon, probably by tidal currents or stirring of the sediments by storms (Flügel 2010). Porostromate oncoids develop preferentially in a

lagoonal setting with low to moderate energy (e.g., Védrine et al. 2007; Pederson et al. 2015). Their smooth surface indicates transport by storms or tidal currents from a nearby area (calm lagoon) to a proximal lagoon, in which they were admixed with ooids. The lack of mud in this step indicates high water energy. As a result, a mixture of components of very different grain size has been formed, characterized also by very different pore sizes (Fig. 10a).

Step 2: First generation of isopachous fibrous cements I (IFC-I) (Fig. 10b)

Early cementation started on the seafloor by precipitation of the first generation of isopachous fibrous cement around all the grains. Isopachous fibrous cements are considered

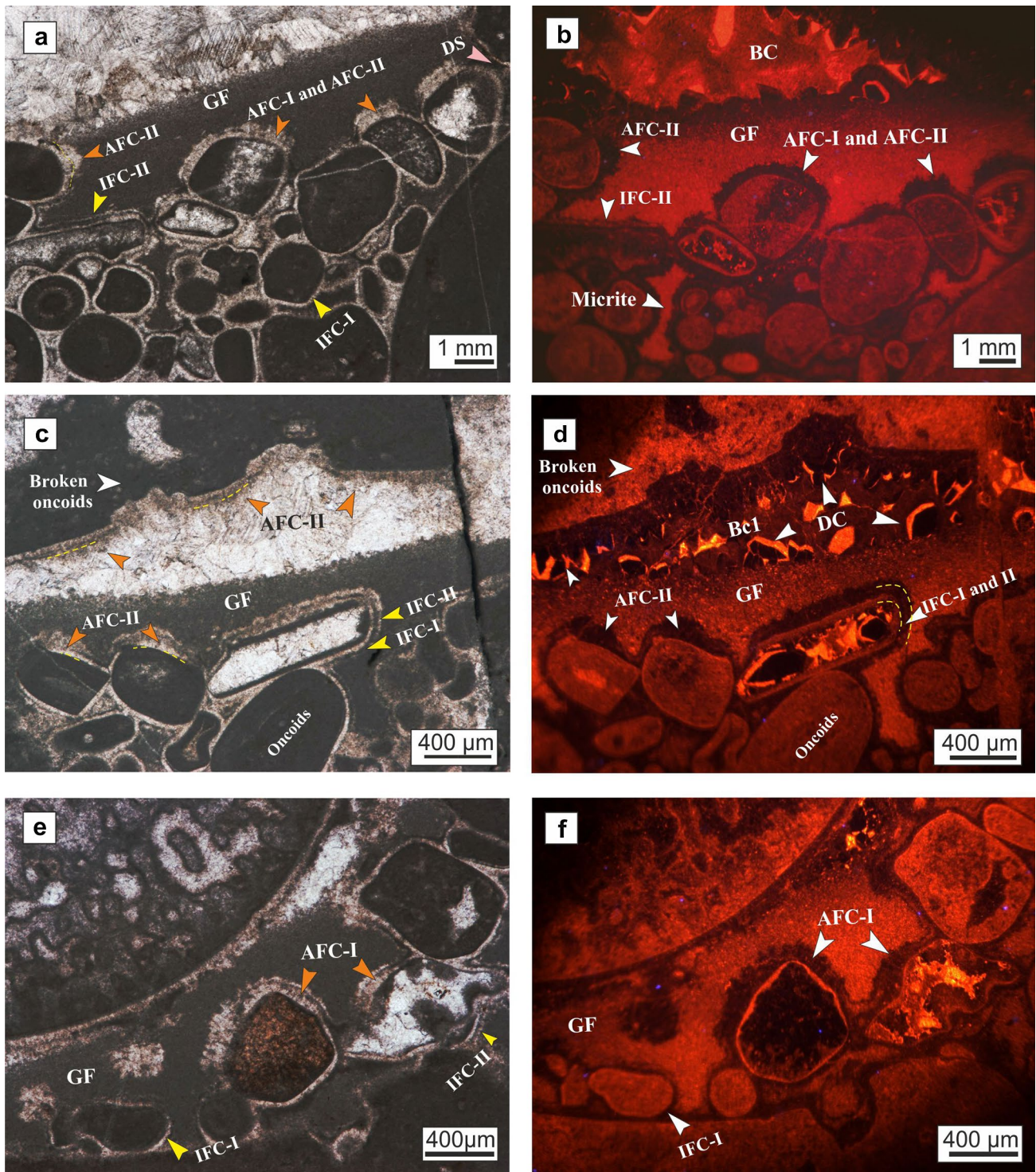


Fig. 6 a Ooidal-oncoidal rudstone showing isopachous fibrous cements I and II (IFC-I and IFC-II), asymmetric cements I and II (AFC-I and AFC-II) and geopetal fabrics (GF). The asymmetric cements nucleate towards the top and in some places from the side towards the pore center. **b** The same sample under CL. Both IFC and AC show no luminescence. The geopetal micrite as well as the

micrite-filled pores exhibit bright luminescence. **c** Oncoidal rudstone showing asymmetric AFC-II cements, nucleating towards the top and from the top towards the bottom. IFC-I and IFC-II are also well preserved. **d** The same sample under CL; no distinction can be made between the AFC-I and AFC-II as both are non-luminescent. **e** AFC-I grown upward. **f** Same as e, under CL, the AFC is non-luminescent

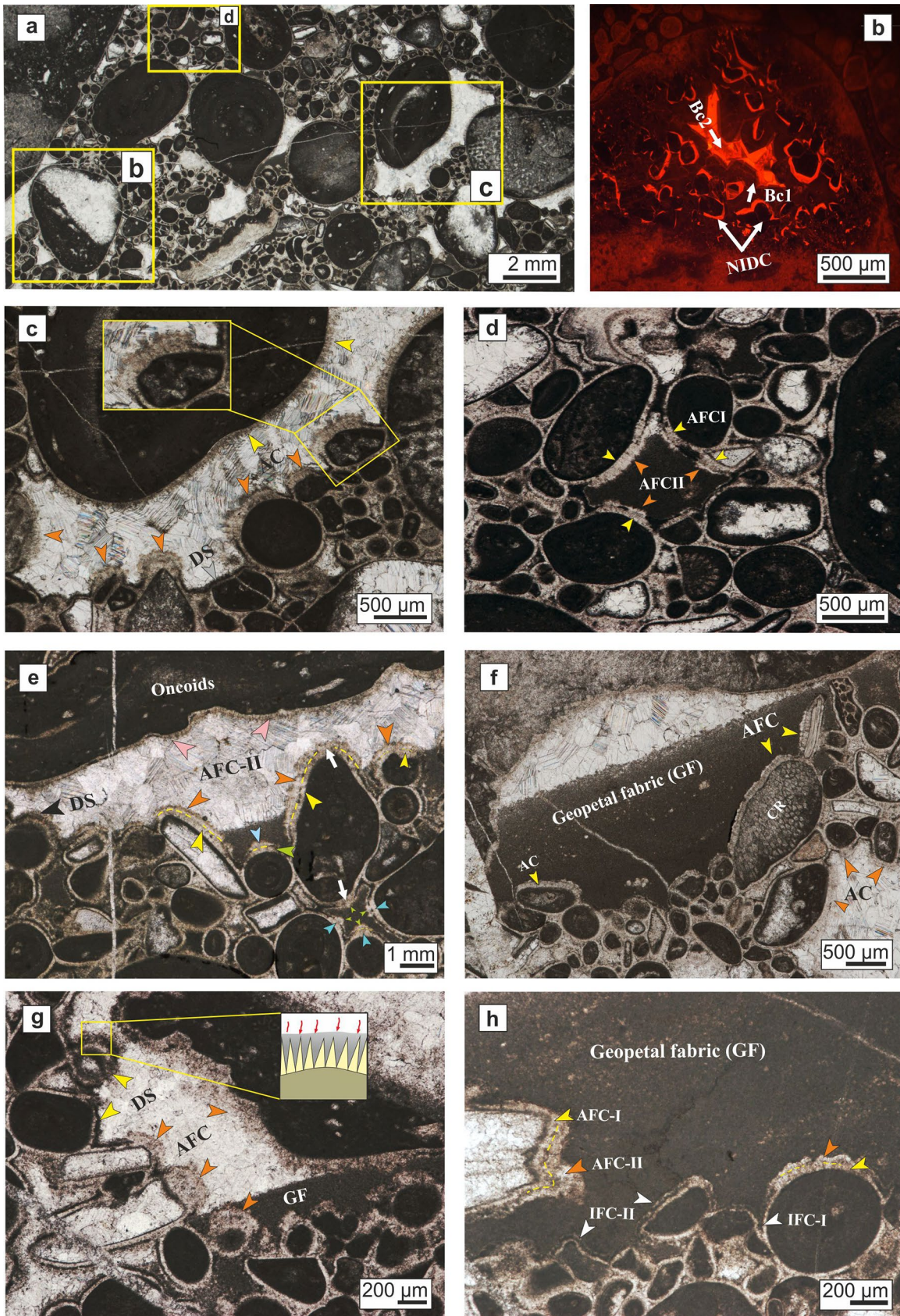


Fig. 7 **a** Oncoids embedded within ooids (rudstone). **b** Original aragonitic shell is replaced first by dogtooth cements (mostly non-luminescent), followed by two generations of granular calcite showing different luminescence (brown and bright). **c** AFC growing towards the pore center. They are well developed on the tops of the exposed sides of small components (orange arrows), but less obvious upon the large exposed component (yellow arrows). **d** AFC-I (yellow arrows) and AFC-II (orange arrows) developed moderately towards the center of a medium-sized pore. **e** The AFC develop preferentially in large and medium-sized pores. The AFC-I (yellow arrows) and AFC-II (orange arrows) grew towards the top and slightly from the bottom upon the large broken oncoids (pink arrows). The almost equal thickness of the cements upon the exposed large grain hides its appearance as AFC. Within the medium-sized pores, AFC-I (blue arrows) and AFC-II (green arrows) are moderately developed, growing from the exposed sides towards the pore center. Upon the same grain (oncoïd), AFC can grow in different directions; they are well developed (thick) facing the large pore, but moderately developed (thinner) when growing into the medium-sized pore (white arrows). **f** AFC developed either more or less upward (yellow arrows), or towards the pore center (orange arrows). Only the geopetal fabrics can emphasize the correct orientation of the thin-section. **g** AFC growing towards the pore center. As in the previous case (c), they are thicker upon the small component. The thin dark sediment (DS) is visible between the cement fibers of the IFC (illustrated in the sketch). **h** Thick AFC-I (yellow arrows) and AFC-II (orange arrows) developed towards the center of a large pore. Note that all thin-section photomicrographs are oriented correctly

as good indicators of the phreatic marine zone (Tucker and Wright 1990; Flügel 2010). Their initial mineralogy is generally aragonite or high magnesium calcite (HMC) precipitated from seawater as fibrous crystals, before being altered to low magnesium calcite (LMC) during later diagenesis (Durllet and Loreau 1996; Knoerich and Mutti 2003; Richter et al. 2003; Andrieu et al. 2018). The pink color of alizarin–potassium ferricyanide stained IFC and the dark luminescence under CL indicate precipitation in well-oxygenated conditions on the seafloor or during very shallow burial (Vincent 2001; Brigaud et al. 2009b). The positive carbon isotope values (median + 0.9‰) are similar to those recorded in the bulk samples of the lagoonal deposits of the logged section (median + 1.1‰; Fig. 3a, b) and also to published middle early Pliensbachian values (Jenkyns et al. 2002; Price et al. 2016). They probably reflect the original $\delta^{13}\text{C}$ values, and thus, confirm their marine nature. However, the negative oxygen isotope values ($\delta - 4.6\text{‰}$) suggest burial conditions for the later alteration of the cements. Permeability is generally high in sand-sized unconsolidated carbonate sediments deposited above fair weather-wave base (Christ et al. 2015) and this holds also for the samples investigated here. High-energy conditions and a low sedimentation rate guarantee seawater renewal in the uppermost porous sediments below the sediment–water interface and thus provide a permanent and sufficient supply of CaCO_3 (Marshall and Ashton 1980; Molenaar and Zijlstra 1997; Coimbra et al. 2009; Christ et al. 2015). In view of the high permeability, the supersaturated seawater could move easily through pores

and trigger calcium carbonate precipitation from the supersaturated seawater (cp. Longman 1980; Tucker and Wright 1990; Molenaar and Venmans 1993), thereby forming the first generation of early cements—the isopachous fibrous cements (IFC-I) (Fig. 10b). Grammer et al. (1999) have shown that sediments on carbonate platforms can lithify by marine cementation rapidly within just a few months. Thus, although probably still in a high-energy environment, precipitation of IFC-I stabilized the sediments on the seafloor, and the grains did not move anymore, forming a slightly lithified seafloor (Christ et al. 2015). Since no bioerosion or epibiotia growing on hard substrate have been observed, it is hard to consider the sediment as a “true” hardground (Hart et al. 2005). However, Brett and Brookfield (1984) showed that near shoals a short phase of seafloor exposure combined with strong seafloor abrasion and erosion is sufficient to form hardgrounds or firmgrounds without ecological effects (epibiotia).

Step 3: First generation of asymmetric fibrous cements (AFC-I) (Fig. 10c)

To our knowledge, so far, no asymmetric cements have been documented that have grown in different directions within a single sample. Instead, asymmetric cements are only known as gravitational cements on the lower side of components, i.e., they are all pointing in the same direction. Such cements can only form in the vadose zone (Purser 1969), either in meteoric environments above the ground water level, or in marine settings immediately above sea level (in beach rocks or intra-/supratidal settings). Gravitational cements have been recorded, e.g., by Müller (1971), Ronchi et al. (2010) and Dickson and Kenter (2014). They were all interpreted as being formed within the diagenetic vadose zone (meteoric or marine) during subaerial exposure, and bound cycles formed during sea-level fall (subaerial unconformity “SU”; e.g., Brigaud et al. 2009a; Smeester et al. 2013; Ritter and Goldstein 2013; Brigaud et al. 2014; Andrieu et al. 2017). Also, in the Ras El Manara section, such acicular pendent cements have been found (Fig. 4b) in a layer at 53 m, ca. 8 m above the layer investigated here (sample 27; Fig. 2a), clearly indicating a marine vadose diagenetic environment.

Although similar to pendant cements at a first glance, the asymmetric cements documented in sample 24 show an important difference to the gravitational cements described above as they have grown in different directions, either upward or towards the pore center. This strongly argues against their formation within the vadose zone and therefore requires a different explanation.

The asymmetric fibrous cements grew on the first generation of isopachous fibrous cements (IFC-I) (Fig. 10c). In contrast to the IFC, which precipitated all around the grains with the same thickness, the AFC-I exhibits a

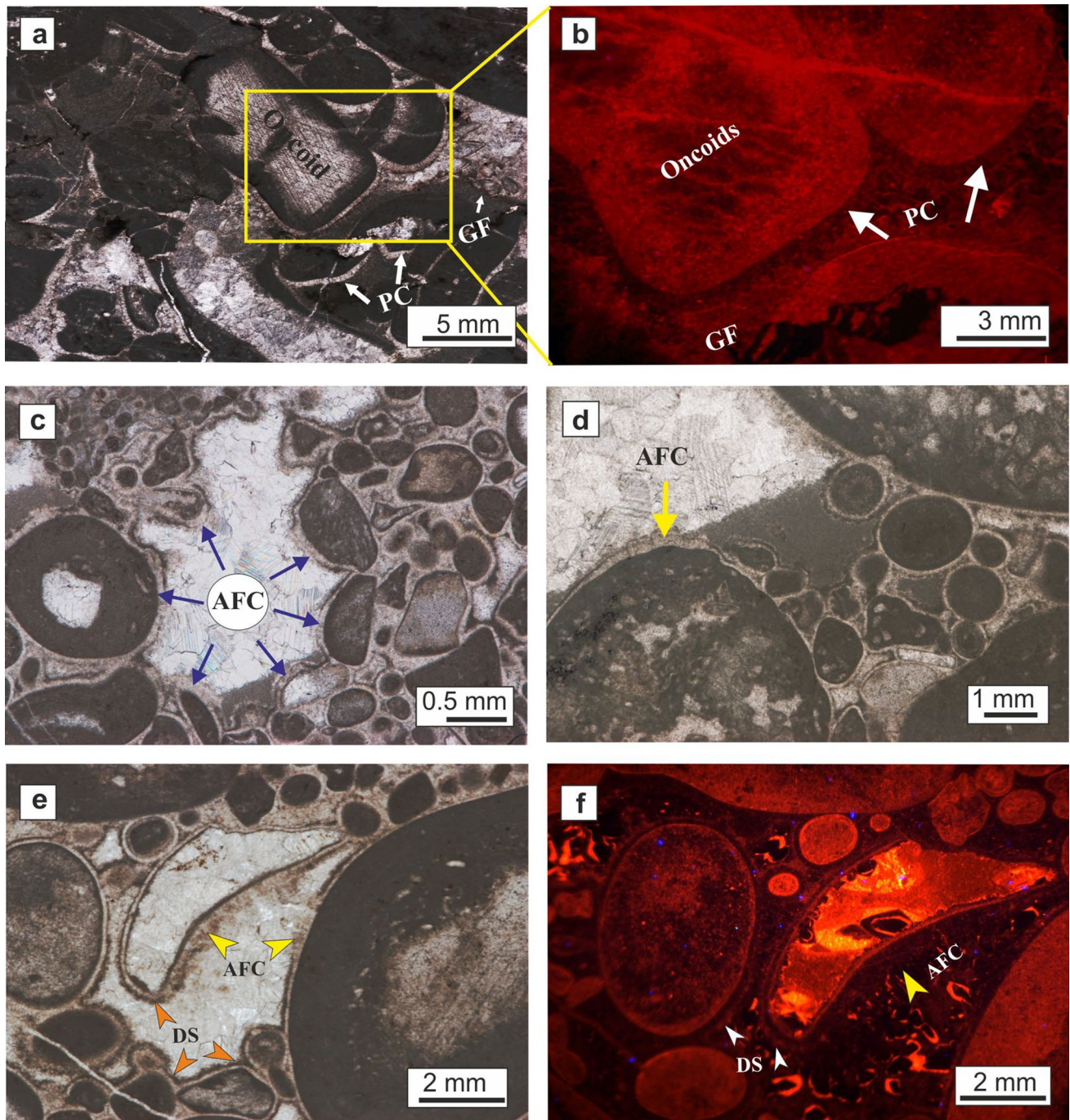


Fig. 8 **a, b** AFC developed in the marine vadose zone (no. 27). **a** Pendant cements (PC), well developed on the bottom of oncoids and oriented in a downward direction. **b** Under CL, they exhibit minor but somewhat patchy luminescence. **c–f** Asymmetric cements developed in the phreatic marine zone (no. 24). **c** The long axes (probably the C axes) of the AFC crystals point towards the pore center (centrip-

etal growth). **d** The long axes of the AFC crystals pointing upward as indicated by the geopetal micrite filling (ascendant growth). **e** The long axes of asymmetric cements are pointing more or less towards the pore center, resembling pendant cements of the vadose zone. **f** Same area as **e**. Under CL, they exhibit a non-luminescence

clear relationship to the pore network of the rock, with the thickest cements growing in the largest pores, and a preferred growth direction toward the center of the pore.

Therefore, the fluid flow conditions within the pore network as well as the pore size must have had a strong influence.

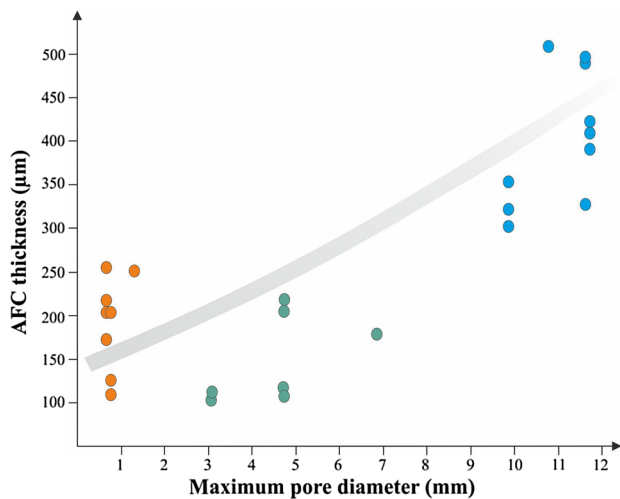


Fig. 9 Relationship between pore diameter and cement thickness of the examples shown in Figs. 6, 7 and 8. Colored dots visualize the trend of thicker fibrous asymmetrical cements in larger pores. Orange dots, small pores; green dots, medium pores; blue dots, large pores

The precipitation rate of carbonate cements in general is determined mostly by the rate of carbonate (CO_3) ion supply to the crystal surfaces (Given and Wilkinson 1985; Niedermayr et al. 2013), and therefore the fluid chemistry plays an important role (Given and Wilkinson 1985). Fibrous or acicular crystals like the ones forming the AFC indicate high Mg/Ca ratios of the fluids as well as rapid precipitation of the crystals (Swart 2015; Christ et al. 2015). High Mg/Ca ratios are typical for marine water, which indicates that the crystals must have formed in very shallow burial conditions where the pores were still filled with seawater. The AFC is non-luminescent, which indicates that the mineralogical transformation from the unstable aragonite or HMC crystals to LMC took place in an oxidizing environment.

Interestingly, these AFC nucleate in a selective way, only upon the exposed sides of grains, which indicates the importance of flow force controlling the rates of fluid exchange at the site of precipitation, as shown by Given and Wilkinson (1985). Godinho et al. (2016) found that the flow within pores is faster in the center and decreases towards the margins (Fig. 11a). Grain surfaces, which are exposed to the center of the pores, therefore experience a stronger pore-water flow than more distant grains (Fig. 11b) and also a higher supply of carbonate ions. Consequently, cement growth can be much faster on the exposed parts of the grains, especially the small ones, resulting in the asymmetry of the cements (Figs. 11c, 12). In contrast, in the pore margins, asymmetric cements are rarely developed (Fig. 11b, c), because of the reduced pore-water flow near the edges of the pores.

The thickest AFC are observed in the biggest pores (Figs. 9, 10). The smaller the pores, the rarer and thinner

are the AFC; in some small pores they are even absent. In fact, a relationship between pore size and cement precipitation (crystallization) has been documented by several authors (e.g., Putnis et al. 1995; Putnis and Mauthe 2001; Emmanuel and Berkowitz 2007; Espinoza-Marzal and Scherer 2010; Putnis 2015; Liu and Jacques 2017). These authors highlighted the fact that precipitation preferentially occurs in larger pores, whereas the small pores can maintain high supersaturation but without crystallization. This is because when fluids circulate from areas of small pores of high supersaturation to large pores, the fluid will lose the equilibrium with regard to the porous matrix, and thereby triggering cement precipitation (Emmanuel and Berkowitz 2007). Another explanation, given by Liu and Jacques (2017), is that when diffusion of the solution is faster in the large pores, precipitation will occur only in large pores, where the supersaturated carbonate solution entered first. This interpretation could support our model, because the first stage of cementation (IFC-I) only slightly reduced the overall permeability but might have (almost) closed the smaller pores, so reducing the fluid flow through them. Consequently, the supersaturated, marine water preferentially circulates through the larger pores, enhancing cement precipitation there.

This interpretation is in accordance with the stable isotope data. The stable carbon and oxygen isotope values from the layer that has clearly experienced subaerial exposure (showing pendant and meniscus cements) exhibit negative carbon isotope values of about -3.8‰ and also negative oxygen values ($\delta^{18}\text{O} = -6.4\text{‰}$; Fig. 3a, b), which could reflect diagenetic stabilization in the meteoric environment, allowing percolation of light, soil-derived CO_2 during the exposure. In contrast, the carbon isotope values of the AFC are mainly positive ($\delta^{13}\text{C} = 1.5\text{‰}$) and are similar to those recorded in isopachous cements of the same sample ($\delta^{13}\text{C} = 0.9\text{‰}$), which argues for formation within the phreatic zone. However, the negative oxygen isotope values ($\delta^{18}\text{O} = -5.7\text{‰}$) suggest recrystallization of the former aragonite or high-magnesium calcite into low-magnesium calcite during shallow burial conditions.

Usually, downward, gravitationally driven water penetration through permeable sands is invoked to explain early CaCO_3 cementation, with isopachous cements in the phreatic zone and with pendant and/or meniscus cements in the vadose zone (e.g., Molenaar and Zijlstra 1997; Christ et al. 2015). However, flow replenishment through a vertical permeability, which is slightly decreased after the first stage of early cementation, cannot explain the growth of the asymmetric cements growing towards the pore centers, and in some places even in the opposite direction of geopetal fabrics (upward). Therefore, horizontal flow of marine waters through pores provides an alternative. But which processes would be responsible for such

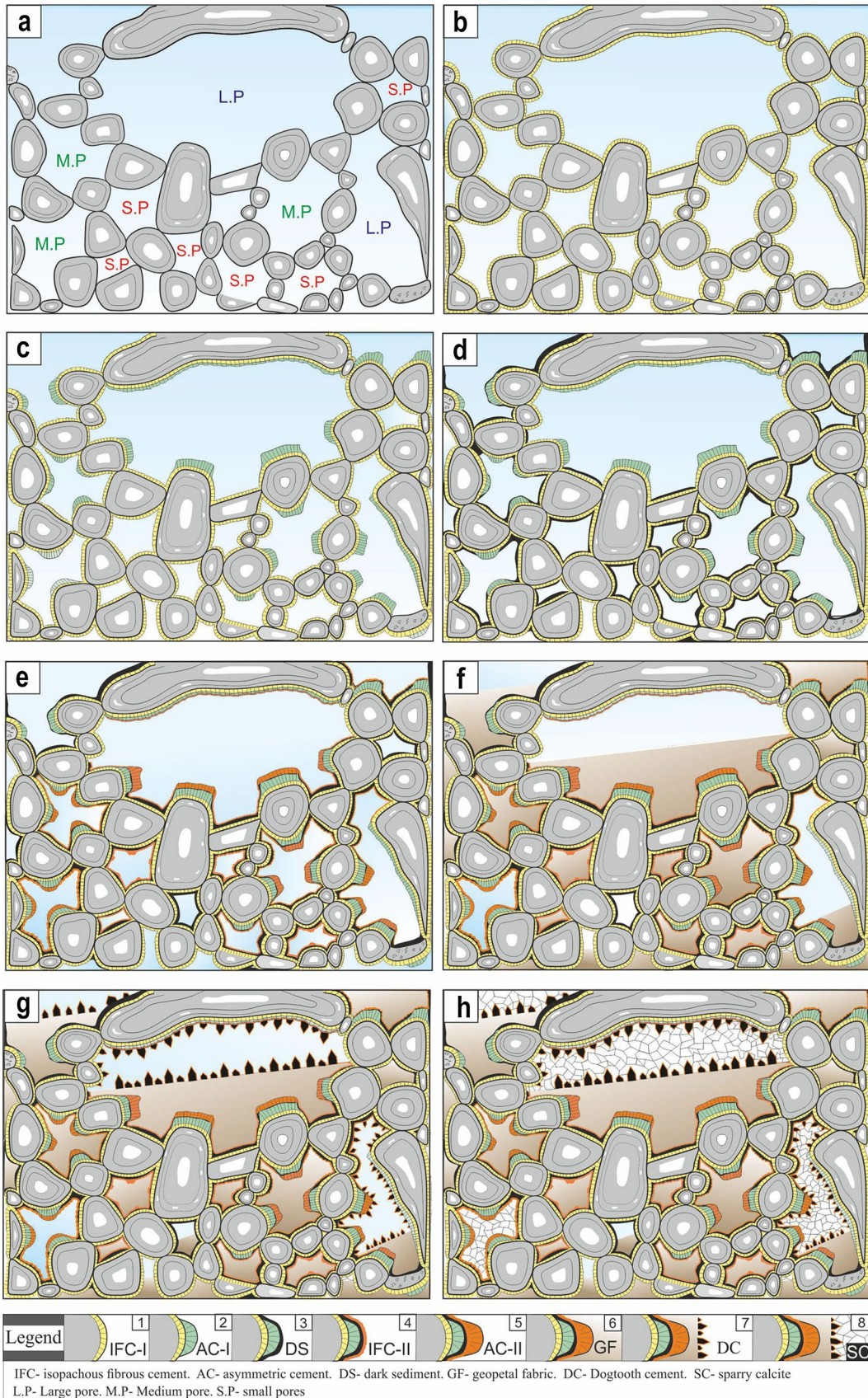


Fig. 10 Sketch showing the different steps of early cementation. **a** Poorly sorted sediment composed of a mixture of ooids, oncoids, and bioclasts. **b** Precipitation of the first generation of isopachous fibrous cement (IFC-I) under high-energy conditions in highly permeable sediment. **c** Formation of the first generation of asymmetric cement (AFC-I) under strong horizontal fluid flow. **d** Small amounts of dark sediment were washed in during a period of calm water-energy. **e** Formation of the second step of isopachous fibrous cement (IFC-II), followed by the second generation of asymmetric cement (AFC-II). **f** Micritic geopetal filling in some pores, which represent the second period of calm energy-water. **g** Generation of dogtooth cements above GF, around grains or filling the moldic pores of bioclasts. **h** Sparry calcite cement filling the remaining pore space. *L.P* large pores, *M.P* medium pores, *S.P* small pores

a horizontal pore-water flow, and why are such cements so rare in the geological record?

We propose the following hypothesis: in intertidal sediments pore-water flow in the shallow subsurface is usually driven by the tides (Pomar et al. 2012; Christ et al. 2015). During low tides, a large part of the water covering the shallow platform during high tides is drained by tidal channels. Depending on the permeability of the sediment, however, a significant part of the water might also flow back through the sediment resulting in a more or less horizontal pore-water flow (Fig. 13). Such a scenario could well explain both the vadose cements in sample 27 as well as the AFC in sample 24. The question why these cements have not been observed so far in other platforms is difficult to answer. It might be related to specific conditions in the investigated carbonate platform allowing the horizontal pore-water flow (sorting, lack of mud) in combination with highly variably pore diameters. It has to be considered also that the maximum vertical pore-water flow per tide is limited by the range of the tides (usually a few meters maximum, commonly less than a meter). In contrast, horizontal pore-water flow can easily be orders of magnitudes higher depending on platform geometry, for example, when passing through a narrow and small shallow area, as the one studied here (Carpman and Leijon 2014). However, it is also possible that such cements are in fact more common but have been overlooked so far. In the samples investigated here the AFC are very obvious because of the subsequent filling of the pores with micritic sediment (Figs. 6, 7).

Step 4: Dark sediment (Fig. 10d)

A thin dark zone is observed between IFC-I and IFC-II (Fig. 6a) and between AFC-I and AFC-II. It probably represents fine sediment, which was flushed into the deposit by slightly turbid, mud-bearing water during a period of less agitated seawater conditions (Fig. 10d). The fine sediment, or at least a fraction of it, was trapped in the space between the needle-shaped crystals of IFC-I or AFC-I (Fig. 7g), or in protected interspaces between components (Figs. 6a, 8e).

Step 5: Second generation of isopachous fibrous cement (IFC-II) (Fig. 10e)

Thin isopachous cement has grown upon the dark sediments, which reflects the return to the high-energy conditions. These cements have been distributed equally around the grains probably by vertical or even horizontal percolation of seawater providing the calcium carbonate (Fig. 10e). However, the minor thickness might be related to moderate hydrodynamic conditions, which provided insufficient carbonate for precipitating thick isopachous cement.

Step 6: Second generation of asymmetric fibrous cements (AFC-II) (Fig. 10e)

Like the first generation, also the second asymmetric cements developed in different directions but usually towards the pore center (Fig. 10e), and therefore grew mostly on top of the first generation of asymmetrical cements (AFC-I) (Fig. 7e), or upon the second thin isopachous cements (Fig. 6a). In view of the fact that the initial grain distribution has been maintained since the first early cementation, this second generation of asymmetric cements nucleates on the same component sides close to the pore center. In addition, AFC-II is thicker in the larger pores compared to the smaller ones, which suggests a similar process of formation as for AFC-I (see above).

Step 7: Formation of micritic geopetal fabrics (GF) (Fig. 10f)

After the precipitation of the IFC and AFC, muddy sediment was flushed into the pore space (Fig. 10f) and filled some of the pores geopetally (e.g., Fig. 7e, f) and others completely (Fig. 7d). The source of this sediment is unclear, as is the environment of its formation. It could have been precipitated from seawater (whittings) and subsequently washed into the open pore space of the slightly cemented rock. However, it also might have been formed during exposure, either from the erosion of a lithified substratum (Aissaoui and Purser 1983), or within small meteoric water lenses (Andrieu et al. 2018). The bright luminescence of both types of micrite suggests the incorporation of Mn^{2+} during lithification (Hiatt and Pufahl 2014), which probably took place in reducing, i.e., oxygen-depleted pore-water during shallow-marine burial diagenesis (cf. Melim et al. 2002).

Step 8: Generation of dogtooth cements (Fig. 10g)

Dogtooth cements (Fig. 10g) can precipitate in a wide variety of environments, from the meteoric to the shallow burial realm (Flügel 2010; Andrieu et al. 2018). The non-luminescence under CL indicates precipitation in

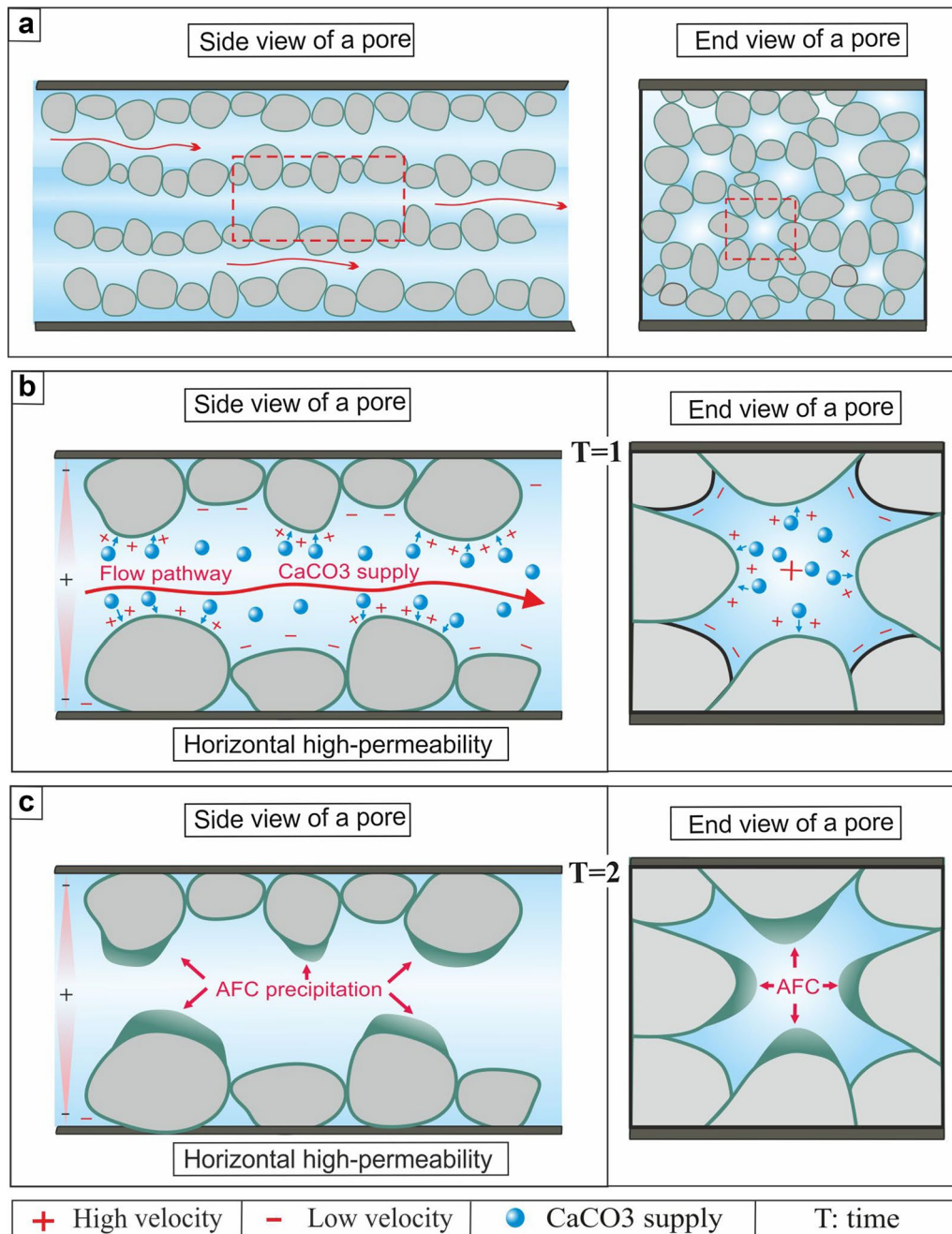


Fig. 11 Strongly simplified sketch showing the pore-water flow. **a** The velocity is highest in the center of the pore within a pore-network. **b** Detail of **a** explaining the mechanism of asymmetric cement development within the phreatic marine zone: the CaCO₃ supply is

much higher within the pore center with its high velocity. **c** Those sides of the component, which are exposed to the pore center are prone to cementation, whereas in the less exposed areas, where the velocity is low, cements are rarely observed

oxidizing water, whereas the bright band at the distal end might indicate either the onset of reducing pore-water conditions during early burial, enabling the incorporation of Mn⁺², or it might reflect variation of redox conditions within the meteoric zone (Godet et al. 2016).

Step 9: Generation of blocky calcite cement (Fig. 10h)

Blocky calcite cements fill the rest of porosity. The first stage which is characterized by brown and bright luminescence

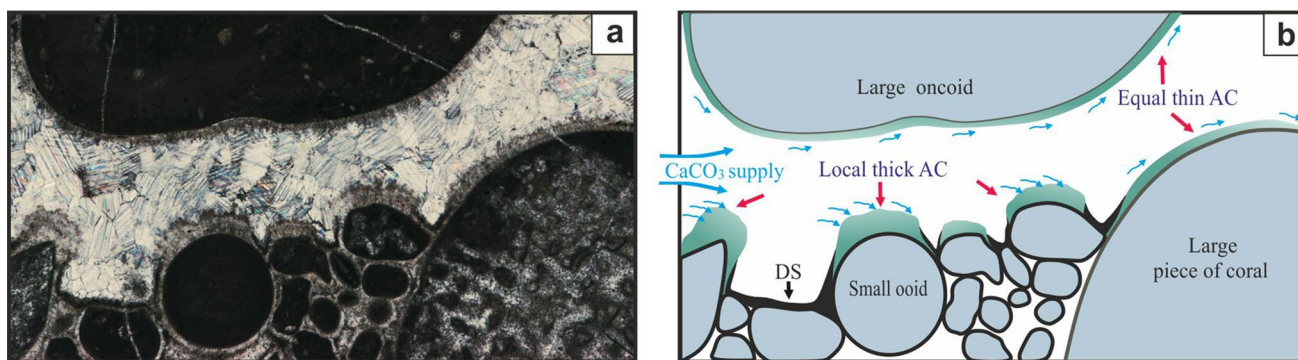


Fig. 12 Distribution of asymmetric fibrous cements (AFC) around different grains. **a** The AFC are thick upon exposed grains (ooids) and thin upon large smooth grain surfaces (oncoids). **b** The CaCO₃ supply (blue arrows) is supposed to be (1) lower and more equally distributed along large, smooth grain surfaces, resulting in thin AFC,

but (2) is locally elevated upon the exposed sides of small grains, giving rise to thick AFC (somewhat similar to a river bank with weak currents (≈ large, smooth component) and a jetty, which is exposed to strong currents (≈ smaller, exposed components))

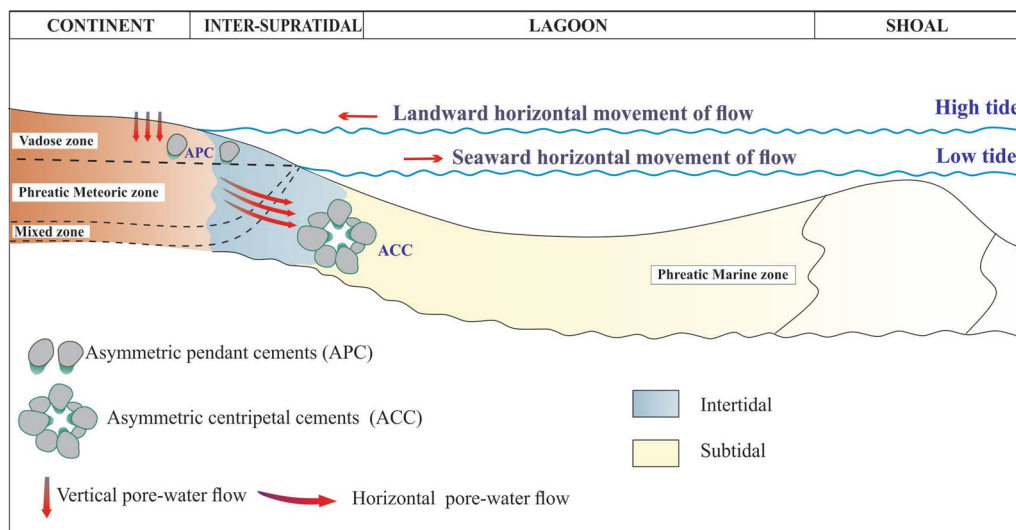


Fig. 13 Sketch explaining the formation of different types of AFC within the vadose zone with vertical pore-water flow (resulting in “true” pendant cements), and in the phreatic zone with horizontal pore-water flow (resulting in non-pendant asymmetrical cements)

(Fig. 7b) indicates proportional incorporation of Mn⁺² and Fe⁺² during precipitation (Fig. 10h). The second stage (Bc2), which is brown in CL indicates oxygen-depleted conditions during the late diagenetic stage, allowing only the incorporation of Fe⁺².

Summary and conclusions

The term asymmetric, non-isopachous cement is commonly used as a synonym for pendant, microstalactitic and gravitational cement, which is routinely used to identify the vadose zone (Flügel 2010; Vuillemin et al. 2011; Csoma and Goldstein 2013; Li et al. 2017; Andrieu et al. 2018). In the present

study, we highlight the fact that asymmetric cement can also be formed within the phreatic zone, under strong horizontal pore-water circulation. In an ideal case, the cement crystals nucleate from different grains and grow preferentially towards the pore center (centripetal growth) (Fig. 14. IIa) or (2) they are developed upon one side, towards the top, forming ascending asymmetric cements (Fig. 14. IIb). In some places (3), they grew downward like pendant cements, and in this case they should be called pendant-like cements (Fig. 14. IIc). As stated above, “true” pendant cements indicate subaerial exposure and thus, e.g., a sequence boundary, formed at the top of a cycle during a relative sea-level drop and exposure. In contrast, the recorded asymmetric cements probably form within an early lithified submerged

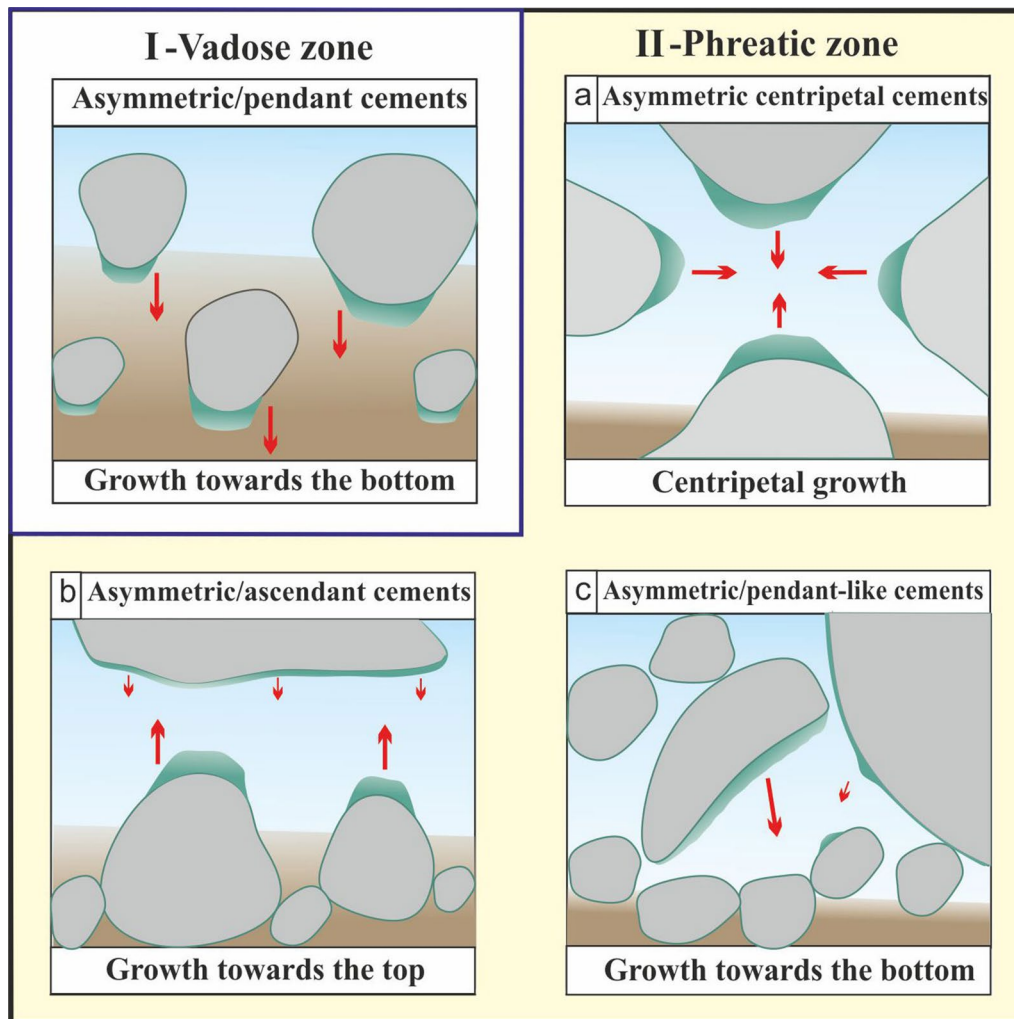


Fig. 14 Different types of asymmetric cements. **I** Asymmetric fibrous cements developed in the marine vadose zone. As a result of vertical drainage, water percolates downward and sticks on the bottom side of components (pendant droplets), then forming asymmetric pendant cements after multiple phases of precipitation and drainage (Fig. 8a). **II** Asymmetric cements developed in the marine phreatic zone. **a** In an ideal case, the asymmetric cements grow towards the pore center

forming asymmetric centripetal cements (Fig. 8c). **b** Similar to **a** but with very different grain sizes, resulting in crust-like cements growing on large, smooth grain and asymmetrical cements growing on smaller grains (Fig. 8d). **c** In some places, asymmetrical cements are developed predominantly downward, but only slightly towards the pore center and resemble real pendant cement, i.e., “pendant-like cements” (Fig. 8e)

substrate (firm-/hardground), and thus might represent a maximum regressive surface (MRS) or maximum flooding surface (MFS) (e.g., Brigaud et al. 2014; Christ et al. 2015; Andrieu et al. 2017). To our knowledge, asymmetric cements as described in the present paper have not been described from elsewhere so far, which means that they are rare. In our case, early marine cementation (IFC-I) played an important role to maintain the pore network and favor AFC precipitation under strong horizontal pore-water circulation.

Our conclusions are as follows:

1. Thin-sections from a Lower Jurassic limestone of the Ras El Manara section (Zailou Formation) in the Traras Mountains (northwest Algeria) reveal cements that at

first glance resemble pendant, gravitational cements. However, these asymmetrical fibrous cements (AFC) are oriented in different directions, locally even upwards, and grew on those grain sides of ooids, oncoids and bioclasts pointing towards the pore centers, ruling out growth in vadose conditions. Such cements have not been described so far from other sections.

2. Petrographic study (polarizing microscope, cathodoluminescence) as well as isotopic data indicate precipitation of the AFC in the marine phreatic zone.

3. A hypothesis is proposed assuming a strong horizontal pore-fluid flow within the marine phreatic zone, probably induced by tides, to be responsible for the AFC,

which nucleate on exposed grains and preferentially grow towards pore centers.

4. Those grain sides, which are close to the pore center, where the flow velocity is highest, receive most CaCO_3 passing through the pores and therefore show the thickest cement. In contrast, in the relatively protected areas at the margins of the pores or in small pores, these asymmetric cements are thin or even absent, because of the more or less stagnant pore-water flow.
5. In terms of sequence stratigraphy, asymmetric pendant cements form generally near the top of sequence during subaerial exposure, whereas the asymmetric cements documented here, which formed within lithified submerged surfaces, could represent a maximum regressive surface or maximum flooding surface. Therefore, especially in samples showing only a few asymmetrical cements, very careful observations are required in order to avoid misinterpretation. Consequently, the terms “pendant”, “microstalactitic” and “gravitational cement” should only be used when a sufficient number of such cements are observed, or when at least the vadose zone is independently confirmed by the presence of other indices such as meniscus cements.
6. The term “asymmetric cements” is not synonymous to pendant cements but includes all types of non-isopachous cements formed either in a vadose or phreatic zone setting.

Acknowledgements This study is a part of the PhD thesis of SB, funded by the Algerian Ministry of Higher Education and Scientific Research. We are very grateful to Birgit Leipner-Mata for preparation of the high-quality thin sections. We thank Michael Joachimski and Mattias López Correa (Erlangen) for their help with the cathodoluminescence and microdrill device, respectively, and Emilia Jarochowska for vivid discussions. We are also very grateful to Jim Hendry and an anonymous reviewer, as well as to editor-in-Chief Maurice Tucker for their critical but very constructive reviews that significantly improved the paper.

References

- Aissaoui DM, Purser BH (1983) Nature and origins of internal sediment in Jurassic limestones of Burgundy (France) and Froud (Algeria). *Sedimentology* 30:273–289
- Ameur M (1999) Histoire d'une plate-forme carbonatée de la marge Sud-Téthysienne: l'autochtone des Traras (Algérie occidentale) du Trias Supérieur jusqu'au Bathonien Moyen: Documents des Laboratoires de Géologie Lyon, France, p 399
- Andrieu S, Brigaud B, Barbarand J, Lasseur E (2017) Linking early diagenesis and sedimentary facies to sequence stratigraphy on a prograding oolitic wedge: the Bathonian of western France (Aquitaine Basin). *Mar Pet Geol* 81:169–195
- Andrieu S, Brigaud B, Barbarand J, Lasseur E (2018) The complex diagenetic history of discontinuities in shallow-marine carbonate rocks: new insights from high-resolution ion microprobe investigation of $\delta^{18}\text{O}$ and $\delta^{13}\text{C}$ of early cements. *Sedimentology* 65(2):360–399
- Brett CE, Brookfield ME (1984) Morphology, faunas and genesis of Ordovician hardgrounds from southern Ontario, Canada. *Palaeogeogr Palaeoclimatol Palaeoecol* 46:233–290
- Brigaud B, Durllet C, Deconinck JF, Vincent B, Pucéat E, Thierry J, Trouiller A (2009a) Facies and climate/environmental changes recorded on a carbonate ramp: a sedimentological and geochemical approach on Middle Jurassic carbonates. *Sediment Geol* 222:181–206
- Brigaud B, Durllet C, Deconinck JF, Vincent B, Thierry J, Trouiller A (2009b) The origin and timing of multiphase cementation in carbonates: impact of regional scale geodynamic events on the Middle Jurassic limestones diagenesis (Paris Basin, France). *Sediment Geol* 222:161–180
- Brigaud B, Vincent B, Durllet C, Deconinck JF, Jobard E, Pickard N, Yven B, Landrein P (2014) Characterization and origin of permeability-porosity heterogeneity in shallow-marine carbonates: from core scale to 3D reservoir dimension (Middle Jurassic, Paris Basin, France). *Mar Petrol Geol* 57:631–651
- Carpman N, Leijon M (2014) Measurements of tidal current velocities in the Folda Fjord, Norway, with the use of a vessel mounted ADCP. In: *Proc ASME 2014 33rd Int Conf Ocean Offshore Arct Eng* 8A: V08AT06A053
- Christ N, Immenhauser A, Wood RA, Darwich K, Niedermayr A (2015) Petrography and environmental controls on the formation of Phanerozoic marine carbonate hardgrounds. *Earth Sci Rev* 151:176–226
- Christ N, Maerz S, Kutschera E, Kwiecien O, Mutti M (2018) Palaeoenvironmental and diagenetic reconstruction of a closed-lacustrine carbonate system—the challenging marginal setting of the Miocene Ries Crater Lake (Germany). *Sedimentology* 65:235–262
- Coimbra R, Immenhauser A, Olóriz F (2009) Matrix micrite $\delta^{13}\text{C}$ and $\delta^{18}\text{O}$ reveals syndepositionary marine lithification in Upper Jurassic Ammonitico Rosso limestones. *Sediment Geol* 219:332–348
- Collin P-Y, Kershaw S, Crasquin-Soleau S, Feng Q (2009) Facies changes and diagenetic processes across the Permian-Triassic boundary event horizon, Great Bank of Guizhou, South China: a controversy of erosion and dissolution. *Sedimentology* 56:677–693
- Csoma AÉ, Goldstein RH (2013) Diagenetic salinity cycles: a link between carbonate diagenesis and sequence stratigraphy. In: Morad S, Ketzer M, de Ros LF (eds) *Linking diagenesis to sequence stratigraphy*. Wiley, New York, pp 407–444
- Dickson JAD (1966) Carbonate identification and genesis as revealed by staining. *J Sediment Res* 36:491–505
- Dickson JAD, Kenter JAM (2014) Diagenetic evolution of selected parasequences across a carbonate platform: late Paleozoic, Tengiz Reservoir, Kazakhstan. *J Sediment Res* 84:664–693
- Durllet C, Loreau JP (1996) Inherent diagenetic sequence of hardgrounds resulting from marine ablation of exposure surfaces. Example of the Burgundy platform, Bajocian (France). *CR Acad Sci Paris* 323:389–396
- Elmi S, Marok A, Sebane A, Almeras Y (2009) Importance of the Mellala section (Traras Mountains, northwestern Algeria) for the correlation of the Pliensbachian–Toarcian boundary. *Volumina Jurassica* 7:37–45
- Emmanuel S, Berkowitz B (2007) Effects of pore-size controlled solubility on reactive transport in heterogeneous rock. *Geophys Res Lett* 34:L06404
- Espinosa-Marzal RM, Scherer G (2010) Advances in understanding damage by salt crystallization. *Acc Chem Res* 43:897–905
- Flügel E (2010) *Microfacies of carbonate rocks: analysis, interpretation and implications*, vol 2. Springer, Berlin

- Given RK, Wilkinson BH (1985) Kinetic control of morphology, composition, and mineralogy of abiogenic sedimentary carbonates. *J Sediment Res* 55(1):109–119
- Godet A, Durlet C, Spangenberg JE, Föllmi KB (2016) Estimating the impact of early diagenesis on isotope records in shallow-marine carbonates: a case study the Urgonian Platform in western Swiss Jura. *Palaeogeogr Palaeoclimatol Palaeoecol* 454:125–138
- Godinho JRA, Gerke KM, Stack AG, Lee PD (2016) The dynamic nature of crystal growth in pores. *Sci Rep* 6:33086
- Grammer GM, Crescini CM, McNeill D, Taylor LH (1999) Quantifying rates of syndepositional marine cementation in deeper platform environments—new insight into a fundamental process. *J Sediment Res* 69(1):202–207
- Guardia P (1975) Géodynamique de la marge alpine du continent africain d'après l'étude de l'Oranie nord-occidentale (Algérie), Relations structurales et paléogéographiques entre Rif externe, le Tell et l'avant pays atlasique. PhD Thesis, Univ Nice, p 289
- Hart MB, Feist SE, Hakansson E, Heinberg C, Price GD, Leng MJ, Watkinson MP (2005) The Cretaceous–Palaeogene boundary succession at StevnsKlint, Denmark: foraminifers and stable isotope stratigraphy. *Palaeogeogr Palaeoclimatol Palaeoecol* 224:6–26
- Hiatt EE, Pufahl PK (2014) Cathodoluminescence petrography of carbonate rocks: applications for understanding diagenesis, reservoir quality, and pore system evolution. In: Coulson (ed) Cathodoluminescence and its Application to Geoscience. Mineral Assoc Can, Short Course Series, V 45, Fredericton, NB, pp 75–96
- Hood AVS, Wallace MW (2012) Synsedimentary diagenesis in a Cryogenian reef complex: ubiquitous marine dolomite precipitation. *Sediment Geol* 324:12–31
- Immenhauser A, Creusen A, Esteban M, Vonhof HB (2000) Recognition and interpretation of polygenic discontinuity surfaces in the Middle Cretaceous Shuaiba, NahrUmr, and Natih Formations of northern Oman. *GeoArabia* 5:299–322
- Jenkyns HC, Jones CE, Gröcke DR, Hesselbo SP, Parkinson DN (2002) Chemostratigraphy of the Jurassic system: applications, limitations and implications for paleoceanography. *J Geol Soc Lond* 159:351–378
- Knoerich A, Mutti M (2003) Controls of facies and sediment composition on the diagenetic pathway of shallow-water heterozoan carbonates: the Oligocene of the Maltese Islands. *Int J Earth Sci* 92:494–510
- Li Z, Goldstein RH, Franseen EK (2017) Meteoric calcite cementation: diagenetic response to relative fall in sea-level and effect on porosity and permeability, Las Negras area, southeastern Spain. *Sediment Geol* 348:1–18
- Liu S, Jacques D (2017) Coupled reactive transport model study of pore size effects on solubility during cement-bicarbonate water interaction. *Chem Geol* 466:588–599
- Longman MW (1980) Carbonate diagenetic textures from near-surface diagenetic environments. *AAPG Bull* 64:461–487
- López-Quirós A, Barbier M, Martín JM, Puga-Bernabéu Á, Guichet X (2016) Diagenetic evolution of Tortonian temperate carbonates close to evaporites in the Granada Basin (SE Spain). *Sediment Geol* 335:180–196
- Marshall JD, Ashton M (1980) Isotopic and trace element evidence for submarine lithification of hardgrounds in the Jurassic of eastern England. *Sedimentology* 27:271–289
- Melim LA, Westphal H, Swart PK, Eberli GP, Munnecke A (2002) Questioning carbonate diagenetic paradigms: evidence from the Neogene of the Bahamas. *Mar Geol* 185:27–53
- Molenaar N, Venmans AAM (1993) Calcium carbonate cementation of sand: a method for producing artificially cemented samples for geotechnical testing and a comparison with natural cementation processes. *Eng Geol* 35:103–122
- Molenaar N, Zijlstra JJP (1997) Differential early diagenetic low-Mg calcite cementation and rhythmic hardground development in Campanian–Maastrichtian chalk. *Sediment Geol* 109:261–281
- Moore CH (2004) Carbonate reservoirs, porosity evolution and diagenesis in a sequence stratigraphic framework. *Dev Sedimentol* 55:444
- Müller G (1971) Gravitational cement: an indicator for the vadose zone of the subaerial diagenetic environment. In: Bricker OP (ed) Carbonate cements. Johns Hopkins University Press, Baltimore, pp 301–302
- Niedermayr A, Köhler S, Dietzel M (2013) Impacts of aqueous carbonate accumulation rate, magnesium and polyaspartic acid on calcium carbonate formation (6–40 °C). *Chem Geol* 340:105–120
- Pederson CL, McNeill DF, Klaus JS, Swart PK (2015) Deposition and diagenesis of marine oncoids: implications for development of carbonate porosity. *J Sediment Res* 85:1323–1333
- Pomar L, Morsilli M, Hallock P, Bádenas B (2012) Internal waves, an under-explored source of turbulence events in the sedimentary record. *Earth-Sci Reviews* 111(1–2):56–81
- Price GD, Baker SJ, Vandeveld J, Clémence ME (2016) High-resolution carbon cycle and seawater temperature evolution during the Jurassic (Sinemurian–Early Pliensbachian). *Geochem Geophys Geosyst* 17:3917–3928
- Purser BH (1969) Syn-sedimentary marine lithification of Middle Jurassic limestones in the Paris Basin. *Sedimentology* 12:205–230
- Putnis A (2015) Transient porosity resulting from fluid–mineral interaction and its consequences. *Rev Mineral Geochem* 80:1–23
- Putnis A, Mauthe G (2001) The effect of pore size on cementation in porous rocks. *Geofluids* 1:37–41
- Putnis A, Prieto M, Fernandez-Diaz L (1995) Fluid supersaturation and crystallization in porous media. *Geol Mag* 132:1–13
- Richter DK, Götze T, Götze J, Neuser RD (2003) Progress in application of cathodoluminescence (CL) in sedimentary petrology. *Mineral Petrol* 79:127–166
- Ritter ME, Goldstein RH (2013) Diagenetic controls on porosity preservation in low stand oolitic and crinoidal carbonates, Mississippian, Kansas and Missouri, USA. In: Morad S, Ketzer M, de Ros LF (eds) Linking diagenesis to sequence stratigraphy. Wiley, New York, pp 379–406
- Ronchi P, Ortenzi A, Borromeo O, Claps M, Zempolich WG (2010) Depositional setting and diagenetic processes and their impact on the reservoir quality in the late Viséan–Bashkirian Kashagan carbonate platform (Pre-Caspian Basin, Kazakhstan). *AAPG Bull* 94:1313–1348
- Sattler U, Immenhauser A, Hillgärtner H, Mateu E (2005) Characterization, lateral variability and lateral extent of discontinuity surfaces on a carbonate platform (Barremian to Lower Aptian, Oman). *Sedimentology* 52:339–361
- Schneidermann N, Harris PM (Eds) (1985) Carbonate Cements. *SEPM Spec Publ*, Tulsa (Oklahoma), USA 36, p 379
- Scholle PA, Ulmer-Scholle DS (2003) A color guide to the petrography of carbonate rocks: grains, textures, porosity, diagenesis. *Am Assoc Petrol Geol*, Tulsa
- Smeester A, Muchez P, Swennen R, Keppens E (2013) Diagenesis at exposure surfaces in a transgressive systems tract in a third-order sequence (Lower Carboniferous, Belgium). In: Morad S, Ketzer JM, De Ros LF (eds) Linking Diagenesis to Sequence Stratigraphy. Wiley, West Sussex, pp 133–150
- Swart PK (2015) The geochemistry of carbonate diagenesis: the past, present and future. *Sedimentology* 62:1233–1304

- Tucker ME, Wright VP (1990) Carbonate sedimentology. Blackwell, Oxford
- Védrine S, Strasser A, Hug W (2007) Oncoid growth and distribution controlled by sea level fluctuations and climate (Late Oxfordian, Swiss Jura Mountains). *Facies* 53:535–552
- Vuillemin A, Ndiaye M, Martini R, Davaud E (2011) Cement stratigraphy: image probes of cathodoluminescent facies. *Swiss J Geosci* 104:55–66
- Vincent B (2001) Sédimentologie et géochimie de la diagenèse des carbonates. Application au Malm de la bordure Est du Bassin de Paris. PhD Thesis, Univ Dijon, p 308